



Repositorio Institucional de la Universidad Autónoma de Madrid

<https://repositorio.uam.es>

Esta es la **versión de autor** del artículo publicado en:

This is an **author produced version** of a paper published in:

ACS Applied Materials & Interfaces 12.4 (2020): 4295-4307

DOI: <https://doi.org/10.1021/acsami.9b20603>

Copyright: © 2020 American Chemical Society

El acceso a la versión del editor puede requerir la suscripción del recurso

Access to the published version may require subscription

Combined Magnetoliposome Formation and Drug Loading in One Step for Efficient AC-Magnetic Field Remote Controlled Drug Release

*Maria Eugenia Fortes Brollo^{*1}, Ana Domínguez-Bajo¹, Andrea Tabero², Vicente Domínguez-Arca³, Victor Gisbert¹, Gerardo Prieto³, Christer Johansson⁴, Ricardo Garcia¹, Angeles Villanueva^{2,5}, María Concepción Serrano¹, María del Puerto Morales^{*1}.*

¹Instituto de Ciencia de Materiales de Madrid, Consejo Superior de Investigaciones Científicas, 28049 Spain. ²Departamento de Biología, Universidad Autónoma de Madrid, 28049 Spain. ³Departamento de Física Aplicada, Universidad de Santiago de Compostela, 15782 Spain. ⁴RISE Research Institutes of Sweden, Göteborg, 41133 Sweden. ⁵IMDEA-Nanociencia, Madrid, 28049 Spain.

ABSTRACT

We have developed a reproducible and facile one step strategy for the synthesis of doxorubicin loaded magnetoliposomes by using a thin-layer evaporation method. Liposomes of around 200 nm were made of 1,2-Dipalmitoyl-sn-glycero-3-phosphocholine (DPPC) and iron oxide nanoparticles (NP) with negative, positive and hydrophobic surfaces that were incorporated outside, inside or between the lipid bilayers, respectively. To characterize how NP are incorporated in liposomes, advanced cryoTEM and atomic force microscope (AFM) techniques have been used. It was observed that only when the NP are attached outside the liposomes, the membrane integrity is preserved (lipid melt transition shifts to 38.7 °C with high enthalpy 34.8 J/g) avoiding the leakage of encapsulated drug while having good colloidal properties and the best heating efficiency under an alternating magnetic field (AMF). These magnetoliposomes were tested with two cancer cell lines, MDA-MB-231 and HeLa cells. First, 100 % of cellular uptake was achieved with a high cell survival (above 80 %), which is preserved (83 %) for doxorubicin loaded magnetoliposomes. Then, we demonstrate that doxorubicin release can be triggered by remote control, using a non-invasive external AMF for 1 hour, leading to a cell survival reduction of 20 %. Magnetic field conditions of 202 kHz and 30 mT seem to be enough to produce an effective heating avoiding drug degradation. In conclusion, these drug loaded magnetoliposomes prepared in one step could be used for drug release on demand at a specific time and place efficiently using an external AMF reducing or even eliminating side effects.

KEYWORDS Superparamagnetic iron oxide nanoparticle, magnetoliposomes, drug delivery carrier, doxorubicin, MDA-MB-231 cells, HeLa cells, magnetic hyperthermia.

INTRODUCTION

Nanotechnology is nowadays offering real solutions to fundamental problems in the pharmaceutical industry. With around fifty products on the market and many more in preclinical and clinical development,^{1, 2} the market is dominated by drug delivery systems, accounting for more than 75 % of the total sales. Thus, it has been widely demonstrated that the effects of a drug can be maximized if a carrier can efficiently deliver it to its target site. This is the case of liposomes, introduced as nanocarriers for doxorubicin (DOX) for breast cancer treatment and being the first nanoformulation approved by the US Food and Drug Administration (FDA) in 1995 (Doxil®). This formulation consists on DOX-loaded liposomes with a size of 80–90 nm coated by PEG to reduce immunogenicity and to prolong plasma half-life. The dose considered safe and effective was reduced to 20 mg/m² from 60 mg/m² for free DOX, also reducing the risk of cardiac events³⁻⁵. DOX molecules drift in and out the liposome through the lipid membrane by simple diffusion. This is the only nanocarrier approved for DOX by any of the regulatory agencies, so far, although many research studies on other nanosized drug carriers based on polymeric or inorganic nanoparticles such as carbon nanotubes, silica, gold and magnetic nanoparticles have been conducted.⁶⁻⁸

Although the usage of liposomes has been shown to increase cell-specific drug accumulation and, in some cases, it is possible a controlled drug release, many scientific challenges lie ahead. For example, the chemistry of nanosized molecules is still not fully understood, and the manufacturing and characterization of such nanocarriers are costly and lack of standardization. Furthermore, much remains to be learned about the modification of nanoscale carriers so that circulation lifetime, biodistribution, penetration of biological tissues and remote control of drug release are optimized. With regard to the last point, drug release by diffusion can be controlled through the liposome formulation that changes the melting (T_M) or phase transition temperature between a fluid and a gel state.⁹⁻¹¹ Thus, above T_M , phospholipids are permeable to water allowing the drug encapsulation, while below T_M , phospholipids are stabilized in a gel state. T_M above body temperature ($T \sim 37^\circ\text{C}$) is required to avoid drug leakage before reaching the site of action but very high T_M results in slow and inefficient drug release by simple diffusion.

In this line, the liposome membrane permeability can be remotely controlled by temperature changes that triggers drug delivery. These can be achieved using a magnetically-triggered approach, by adding magnetic nanoparticles to the liposomes and then, applying an alternate magnetic field to heat the particles.¹²⁻¹⁴ Changes in pH can also alter the membrane permeability of liposomes but they cannot be remotely induced.¹⁵ Gold was also used to control drug release from liposomes using a laser to heat the particles but with low tissue penetration, being in the order of 10 mm.¹⁶ The combination of liposomes and magnetic NP leads to magnetoliposomes, which are promising nanocarriers for directing drugs to specific tissues and organs, avoiding the side effects of current treatments. Magnetic NP can also be tracked in biological matrices allowing their in-vivo monitorization by magnetic resonance imaging (MRI).^{17, 18} The main challenge in this area is the incorporation of the NP without compromising liposome membrane integrity and avoiding the leakage of encapsulated compounds. On the other hand, controlled release should rely on a local or nanoscale heating mechanism, where the NP transfer heat to the liposome and cause a phase change within the bilayer that triggers permeabilization.⁹ The local heating should not increase the bulk temperature to avoid degradation of the drug.¹⁹

Here, we have developed a reproducible strategy for the synthesis of magnetoliposomes with controlled liposome size and analyzed the effect of different nanoparticle spatial distribution around the liposome on its membrane integrity, along with their colloidal, magnetic and heating properties. We have evaluated the use of these magnetoliposomes as drug delivery carriers using DOX applied to MDA-MB-231 and HeLa cells. While HeLa is a cell line derived from cervical cancer cells remarkably durable and prolific and extensively used in scientific research, MDA-MB-231 cell line is used in *in-vitro* models of triple-negative breast cancer (estrogen receptor negative (ER- α), progesterone receptor negative (PR) and HER-2 negative), which corresponds to one of the most aggressive, therapy-resistant and metastatic tumors.^{20,21} We have analyzed cellular uptake of magnetoliposomes and their therapeutic effect when loaded with DOX by studying cell viability and proliferation. We have also studied the controlled mechanism for drug release on demand using an external AMF. These magnetoliposomes could be used as models mimicking cell

membranes to study cell-nanoparticle interactions and the heat effect of AMF, using the lipid bilayer fluidity as a sensor for temperature changes. The ability to safely track these magnetoliposomes by MRI is extremely important to potentially monitor long-term treatments.

RESULTS

Uniform magnetoliposomes of around 200 nm have been synthesized by the thin-layer evaporation method. The spatial distribution of the nanoparticles in the liposome can be controlled by changing the nanoparticles coating. Here, 15 nm core iron oxide nanoparticles with three different coatings were used: DMSA (negatively charged), APS (positively charged) and oleic acid (hydrophobic). The structures that result of this study can be seen in figure 1A: NP attached to the liposome surface (DMSA coating), NP encapsulated in its aqueous volume (APS coating), NP inside the lipid bilayer (oleic acid coating) and liposomes without any nanoparticles (figure S1A). For comparison it was used a commercial cationic liposome (positive surface charge), where the NP are encapsulated in its aqueous volume (DMSA coating) (figure S1B). Synthesis procedure reproducibility for three replicate samples showing magnetoliposome mean size and size distribution calculated by transmission electron microscopy and dynamic light scattering can be seen in figure S2.

Surface charge of the magnetoliposomes gives an idea of the spatial distribution of the particles in the liposomes (figure 1B). Only the magnetoliposomes with DMSA coated NP have a high negative surface charge of around -15 mV, which supports the fact that the NP are indeed attached at the surface of the liposome, assuring its colloidal stability at pH 7. On the contrary, liposome without nanoparticles and magnetoliposomes with oleic acid coated NP and APS coated has a negative surface charge of around -3 mV, as expected for DPPC lipids (figure 1B).²² Which supports the fact that these NP are inside the lipid bilayer (Oleic) or inside the aqueous part (APS) of the liposomes, respectively, as seen in figure 1A. The low surface charge of these magnetoliposomes limits its colloidal stability. The surface charge of DMSA coated NP is highly negative, at around -30 mV, while for APS coated NP is highly positive, at around +30 mV.

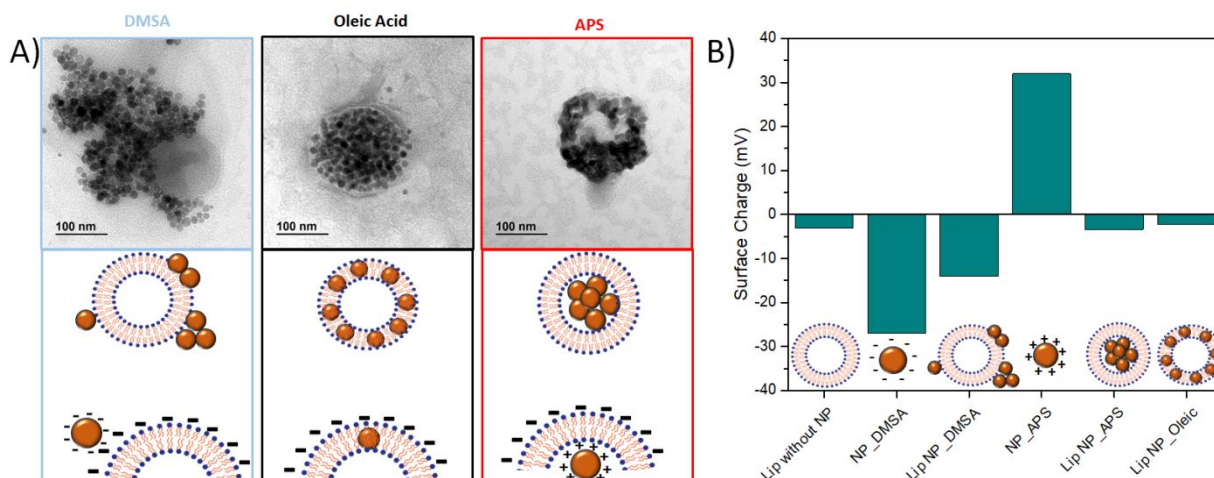


Figure 1. A) TEM images and corresponding schemes of liposomes produced with nanoparticles using different coatings as DMSA (blue), oleic acid (black) and APS (red), resulting in different nanoparticles spatial configurations. B) Zeta potential measurements at pH 7 for these magnetoliposomes and the comparison with free nanoparticles.

Similar results were obtained for smaller particles reinforcing the idea that the coating controls the spatial distribution of the particles in the liposome. Thus, 8 nm particles are encapsulated inside the lipid bilayer when coated by oleic acid and attached at the liposome surface when coated with DMSA as observed by TEM (figure S3, figure S4).

Calorimetric measurements (figure 2 A and B) show that the melt transition peak changes by the incorporation of the nanoparticles in the liposomes. DPPC has a peak at 41.6 °C, with enthalpy of 38.6 J/g (figure 2A orange curve). Incorporating 15 nm NP coated by DMSA shifted the peak to 38.7 °C, with enthalpy of 34.8 J/g (figure 2A blue continuous curve). Smaller DMSA coated NP has shifted the main peak to 40 °C, with enthalpy of 31.8 J/g (figure 2A, blue dashed curve). These variations in the melting temperature support that these NP are attached at the surface of the liposomes perturbing slightly the lipid bilayer. It should be noted that larger particles provoke a larger shift in the melting temperature probably as a consequence of the pressure on the lipid bilayer membrane or changes in membrane rigidity that will depend on the contact area between the liposome and NP surface. However, when incorporating NP covered by oleic acid (8 and 15 nm), the main peak is shifted to even lower temperatures, 38.4 °C and 38.6 °C with a significant broadening and enthalpies of 27.8 J/g and 23.2 J/g, respectively (figure 2B), given the substantial perturbation of the lipid bilayer, as previously observed.²³ Similar variations in the melting temperature (from 40.4 °C to 38.8 °C) were reported for gold and silver nanoparticles of around 3 to 6 nm inside the lipid bilayer.²⁴⁻²⁶ It should be emphasized that choosing phospholipids with gel states at physiological conditions is desirable for biomedical applications, and in particular for drug delivery to avoid leakage in circulation. Therefore, nanoparticles coated with DMSA were chosen in this work to decorate the liposomes surface, given that its main transition is above body temperatures (38.7 °C). In addition, these magnetoliposomes show high enthalpy (34.8 J/g)

assuring that they are less fragile than those containing oleic acid coated nanoparticles inside the bilayer.

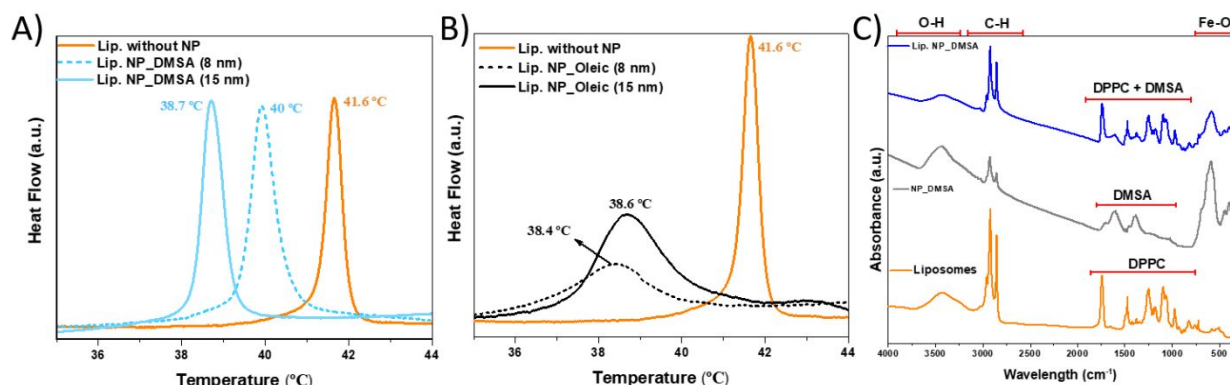


Figure 2. DSC measurements of DPPC lipid membranes, A) with nanoparticles coated by DMSA with different core sizes (8 nm dashed line and 15 nm continuous line), B) with nanoparticles coated by oleic acid with different core size (8 nm dashed line and 15 nm continuous line), where the shift of the peak is proportional to the lipid membrane perturbation. Liposomes without particles are also shown for comparison (orange curves). Pre-transition peak is not observed. C) Infrared spectra of nanoparticles coated by DMSA (gray curve), liposomes without nanoparticles (orange curve) and magnetoliposomes with DMSA coated nanoparticles (blue curve).

Supporting the idea that the liposome membrane integrity is preserved when DMSA coated nanoparticles are attached at the surface, we observed that DPPC infrared bands were not affected by the incorporation of the particles (figure 2C). The typical bands for water above 3100 cm^{-1} , antisymmetric and symmetric CH stretching between 3000 and 2500 cm^{-1} and signature bands for DPPC phospholipids below 2000 cm^{-1} can be seen in the case of liposomes (orange curve) and magnetoliposomes (blue curve).²³ DPPC and magnetoliposomes show similar bands at 1730 cm^{-1} due to C=O bond, in the region 1469 – 1439 cm^{-1} mainly due to C-H deformation modes from the lipid acyl chains, asymmetric CH_3 stretching mode at around 1377 cm^{-1} and asymmetric and symmetric stretching modes for the PO_2^- group near 1250 cm^{-1} and 1085 cm^{-1} , respectively. Between 1700 and 1000 cm^{-1} , bands for the DMSA coating appear for free nanoparticles (gray curve): at 1640 cm^{-1} due to the vibration of the C=O bond, at 1450 cm^{-1} due to bending of CH bond and at 1140 and 1000 cm^{-1} broad absorption bands appear owing to the vibration of the S-CH bond. Finally, bands below 1000 cm^{-1} are associated with the vibration modes of the iron oxide, Fe-O stretching,²⁷ appearing in the curve of free nanoparticles (gray) and magnetoliposomes (blue).

In order to optimize nanoparticle size and magnetic field conditions to overcome the liposome melting transition, heat efficiency of free nanoparticles and magnetoliposomes were tested from their Specific Absorption Rate (SAR). Three field configurations were used: 92 kHz ($65\text{ mT} = 52\text{ kAm}^{-1}$), 202 kHz ($30\text{ mT} = 24\text{ kAm}^{-1}$) and 282 kHz ($21\text{ mT} = 17\text{ kAm}^{-1}$) and two core sizes (8 and 15 nm), seen in figure 3A. For free NP, the larger the core size greater its efficiency to generate heat, for a determined field condition, as already known from the literature.^{28, 29} The best field

configuration for these samples is clearly 202 kHz giving the highest SAR values for both sizes, 49 W/gFe for 8 nm nanoparticle ($\Delta T = 3.9$ °C) and 265 W/gFe for 15 nm nanoparticle ($\Delta T = 8.4$ °C). Comparing with bibliographic data iron oxide nanoparticles of small core size nanoparticles achieved SAR values around 37 W/gFe for high frequencies³⁰ and around 15 W/gFe for low frequencies.^{31,32} Experimentally, large nanoparticles have SAR values around 150 W/gFe³³ up to 900 W/gFe.³⁴ However, theoretical prediction of the linear response theory (LRT) for an AC field of $H = 36.5$ kAm⁻¹ and $f = 341$ kHz, and iron oxide nanoparticles of around 22 nm gives a SAR of 500 W/gFe.³⁵ Aggregation or self-assembly processes forming chain for example may be responsible for SAR enhancement.³⁶

Magnetoliposomes containing 8 and 15 nm nanoparticles present lower SAR values (42 W/gFe and 98 W/gFe) than the corresponding free NP (figure 3B), with $\Delta T = 2.4$ and 3.2 °C respectively. These SAR values are expected to increase up to 400 W/g if using high frequency field such as 700 kHz,³⁷ but then the conditions would not fit the bio requirements.³⁸ It is also observed in figure 3B that for 8 nm NP there is only a slight difference in heat efficiency after the encapsulation, while for 15 nm nanoparticles SAR efficiency drops extensively. A reduction of 63 % in SAR in the last case is then related to the immobilization of the nanoparticles in the liposomes, in agreement with the reported data for 15 nm NP dispersed in a hydrogel.³⁹ In spite of that SAR reduction, the increase in temperature produced by the AMF seems to be enough to overcome the melting transition of these magnetoliposomes containing 15 nm NP attached at the liposome surface. In addition, field conditions such as 202 kHz and 30 mT seem to be enough to produce an effective magnetic hyperthermia. NP will then transfer the heat directly to the lipid bilayer producing a local heat and not necessarily increasing the bulk temperature.¹⁹

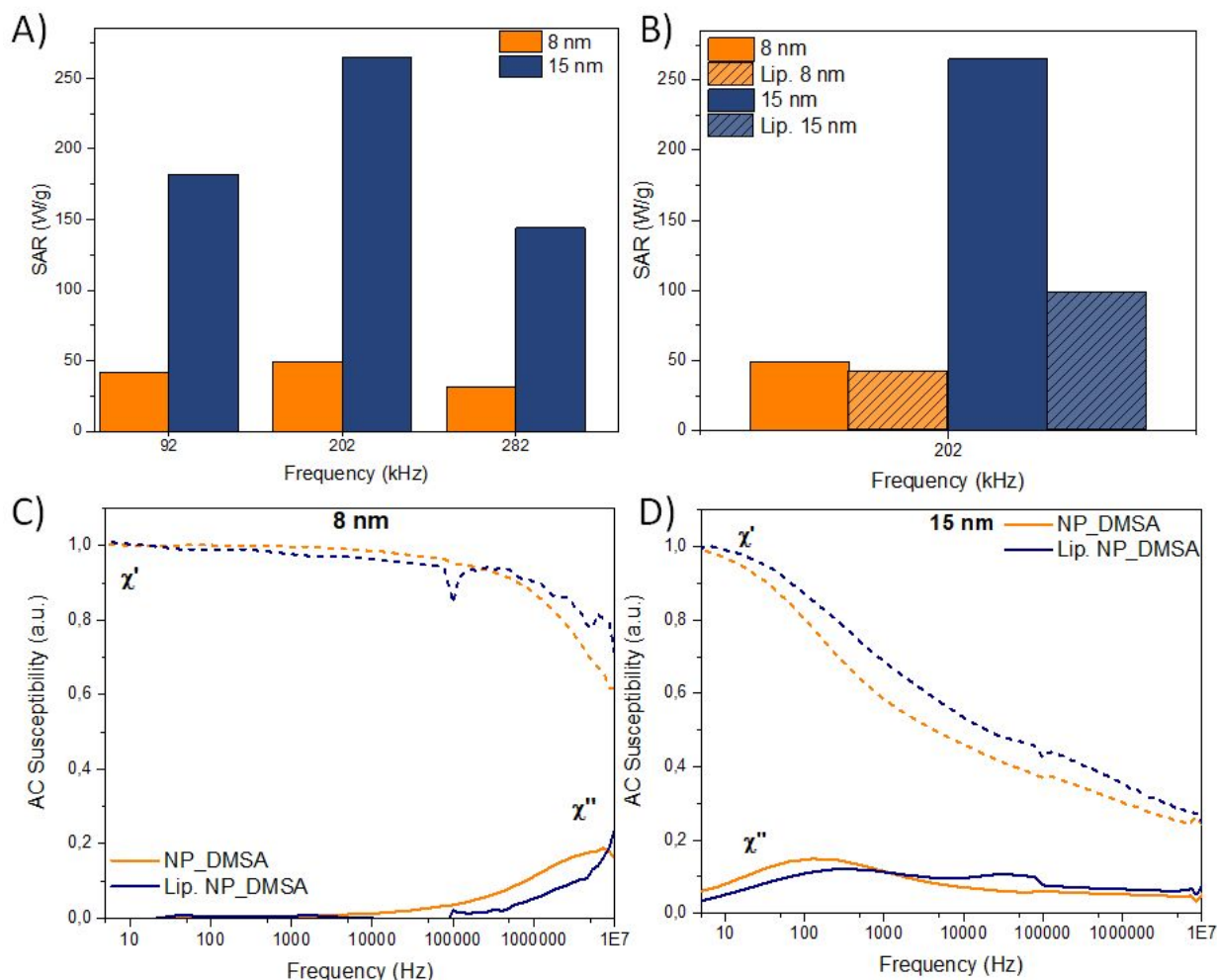


Figure 3. A) SAR values for NP of 8 and 15 nm at 92, 202 and 282 kHz. B) SAR values for NP of 8 and 15 nm at 202 kHz and 30 mT and their respective magnetoliposomes. All samples were measured at a concentration of 1.5 mgFe/ml. Below there is a frequency dependence of the low-field mass AC susceptibility showing the real part χ' (dashed lines) and the imaginary part χ'' (continuous lines) for DMSA-coated NP (orange curves) or magnetoliposomes with DMSA-coated NP (blue curves) for small nanoparticles of 8 nm (C) and larger nanoparticles of 15 nm (D). To facilitate comparisons, data were normalized such that the maximum χ' values were unity in each case. The leap around 10⁵ Hz is given by the fusion of data acquired by two different AC susceptometers.

The origin of the heat production is the rapid change in the direction of particle magnetic moments through Néel or Brown relaxation losses, where the first one is preferred for biomedical applications since it is independent on the media viscosity.⁴⁰ The results of the AC susceptibility versus frequency shown in figure 3, give evidence that the small sized nanoparticles exhibit Néel relaxation (figure 3C), independent on being or not physically connected to the liposome (maximum of the out-of-phase susceptibility component χ'' appears to be above 10 MHz, and a non-zero value of the real part of the AC susceptibility even at 10 MHz). On the other hand, the 15 nm nanoparticles have both Néel and Brownian relaxation behavior (a relaxation peak in the out-of-phase component at about 130 Hz) (figure 3D). Therefore, when these 15 nm NP are

physically attached to the liposome, Néel mechanism will contribute more to the heating, since it is nonviable for the whole magnetoliposome to physically rotate due to its large hydrodynamic size. The shift in frequency of the relaxation peak and the broadening of the out-of-phase component can be related to the effect on interaction between nanoparticles when they are encapsulated in liposomes and by the polydispersity of the sample.^{41, 42} These results support the previous drop observed in the SAR values for 15 nm magnetoliposomes (figure 3B). From the AC susceptibility measurements on dilutions of the samples it was found that the relaxation frequencies were constant with particle concentration, indicating that there is no evidence of interactions between the particles in the dynamic magnetic response.⁴¹

To further evaluate how the NP are incorporated into the liposomes it has been applied bimodal atomic force microscopy (AFM), figure 4. Bimodal AFM is a nanoscale characterization method that identifies the components of a heterogeneous interface based on their nanomechanical response.⁴³⁻⁴⁵ A solution of liposomes was deposited on a mica surface and the adsorbed liposomes were imaged in water. Figure 4A shows an AFM topography image of several liposomes (without NP) deposited on mica. The liposomes have a sphere-like structure with diameters ranging between 20 and 200 nm. Figure 4B shows an AFM topography image of a liposome loaded with NP coated by DMSA. The liposome shows a non-spherical geometry with several features protruding from the surface. By imaging larger area of this sample (data not shown) it was concluded that the liposome is adsorbed on a lipid bilayer. This bilayer outside the liposome covers the mica surface. This layer was formed on the mica during the liposome deposition. Bimodal AFM enables to characterize the topography of the liposomes simultaneously with the mapping of different nanomechanical properties. The nanomechanical map (figure 4C) shows local variations across the liposome-water interface. The presence of single and NP clusters outside the liposome facilitates the association of the nanomechanical contrast with the NP structure. For example, several single NP are observed at the far right of the image. By using the bimodal compositional contrast given by the NP observed on the lipid bilayer outside the liposome it can be located the positions and structure of the NP associated with the liposome. Figure 4D shows a scheme of the NP structures observed on the lipid bilayer and the liposome. The schemes are overlaid with the bimodal map (figure 4C) to generate a map identifying the NP structures associated with the liposome (figure 4E). Five different NP structures are observed as an isolated NP on top of the lipid bilayer, an isolated NP just underneath the surface, a NP buried within the lipid bilayer, a NP cluster on top of the lipid bilayer and mixture of lipids and NP. The incorporation of the NP in the liposome is expected to increase the local stiffness of the regions with NP (data not shown). This result is consistent with previous force-volume measurements performed on lipid bilayers loaded with NP that showed an increase of the Young's modulus of the bilayer.⁴⁶ In these experiments, to avoid the unwanted rupture of the liposome membrane it has been applied a maximum indentation of 1.5 nm. As consequence, the experiments do not provide information on the water core region of the liposome.

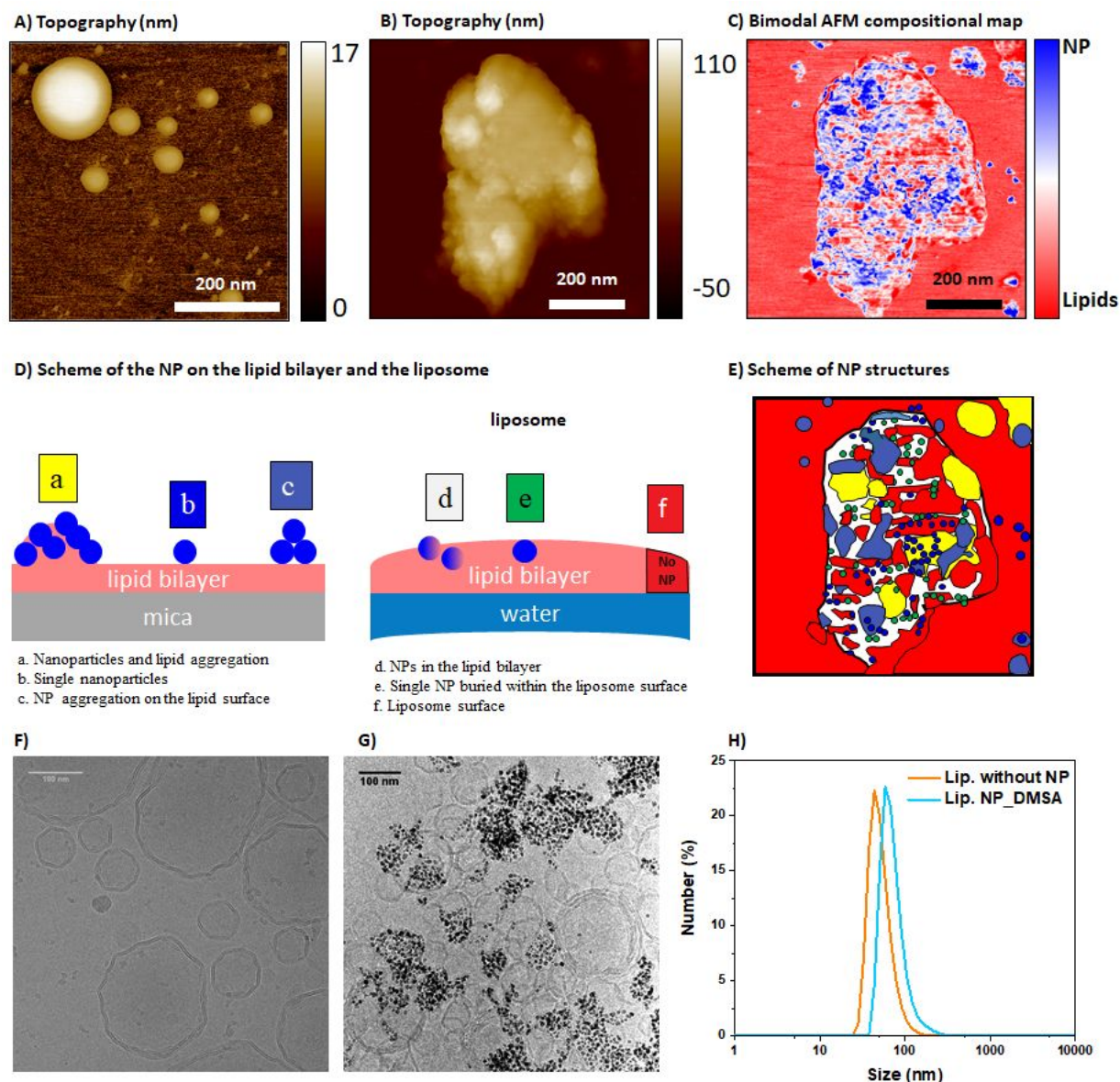


Figure 4: Bimodal AFM maps of large NP on liposomes. (A) Amplitude-modulation AFM image (topography) of liposomes without nanoparticles deposited on mica. (B) Bimodal AFM image (topography) of a DMSA coated nanoparticle attached to the liposome, where the liposome rests on top of a lipid bilayer adsorbed on mica. (C) Bimodal AFM compositional map. The local nanomechanical interactions between the tip and sample enable to identify the positions of the NP on the liposome and the lipid bilayer. (D) Scheme of different NP structures on the lipid bilayer and liposome. (E) Map of the different NP structures found on the lipid bilayer and liposome. The map is deduced from the bimodal AFM compositional map shown in (C). All the images have been taken in water. (F) Cryo-TEM images of liposomes without nanoparticles, revealing mostly spherical unilamellar vesicles. (G) Cryo-TEM images of magnetoliposomes with large DMSA-coated NP, some multilamellar vesicles are also present. (H) Hydrodynamic size in number distribution for plain liposomes and magnetoliposomes.

Finally, Cryo-TEM was used to observe the liposome with intact morphology, as its real size, shape and lamellarity. Figure 4F shows liposomes without any nanoparticles, revealing unilamellar

vesicles of around 100-200 nm. Figure 4G shows liposomes with DMSA coated nanoparticles (15 nm) where some multilamellar vesicles are also present, in less extent. The frozen samples are highly sensitive to the radiation so are viewed under low dose conditions to avoid electron beam damage. Hydrodynamic sizes measured by DLS are adjusted to a monomodal distribution with mean values around 60 nm ($PDI < 0.2$) in both cases (figure 4H).

Biocompatibility tests were carried out *in-vitro* with MDA-MB-231 (human breast cancer) and HeLa (human cervical cancer) cells (supporting information). MDA-MB-231 cell line is one of the most used *in-vitro* models for triple-negative breast cancer.²⁰ Cell uptake after exposure for 24 h to 0.1 mg Fe/ml concentration led to a high labelling efficiency as can be observed by Prussian blue staining (figure 5). NP and magnetoliposomes were able to enter and accumulate in the cell cytoplasm, but only magnetoliposomes allowed for a 100 % labelling efficiency.

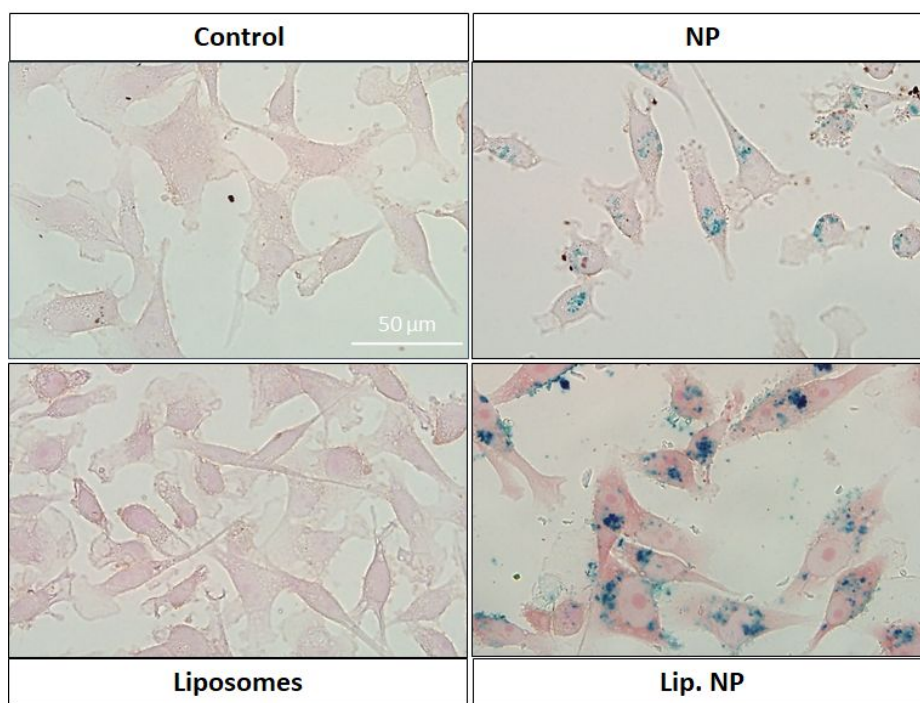


Figure 5. MDA-MB-231 cells incubated for 24 h with plain liposomes, magnetic NP and magnetoliposomes. Cells stained with Prussian blue reaction for iron oxide detection. In all images, scale bar represents 50 μm .

To assess the effect of magnetoliposome on cell viability and proliferation, an MTT assay was performed at two different concentrations: 0.05 and 0.1 mgFe/ml (figure 6A). Cells exposed to NP showed a survival fraction above 90 % with the highest concentrations of Fe, while cells with magnetoliposomes showed a survival fraction above 80 % when compared to the control. Bare liposomes do not present toxicity at concentrations below 4 mM⁴⁷ and when used fresh (first 10 days after synthesis). After that time, some toxicity appears due to lipid degradation.⁴⁸ Interestingly, the application of an AMF did not increase materials toxicity (figure 6B), meaning that cell death by magnetic hyperthermia is not triggered under these conditions. ICP analysis

revealed an increase of almost seven times in the amount of iron uptaken by the cells when incubated with magnetoliposomes, going from around 3 pgFe/cell for free NP to more than 20 pgFe/cell for magnetoliposomes (figure 6C). The internalization of negatively charged NP and magnetoliposomes has been previously observed in intracellular vesicles (namely endosomes).³⁷ Positively charged NP are typically more effective, but lead to higher toxicity levels.⁴⁹

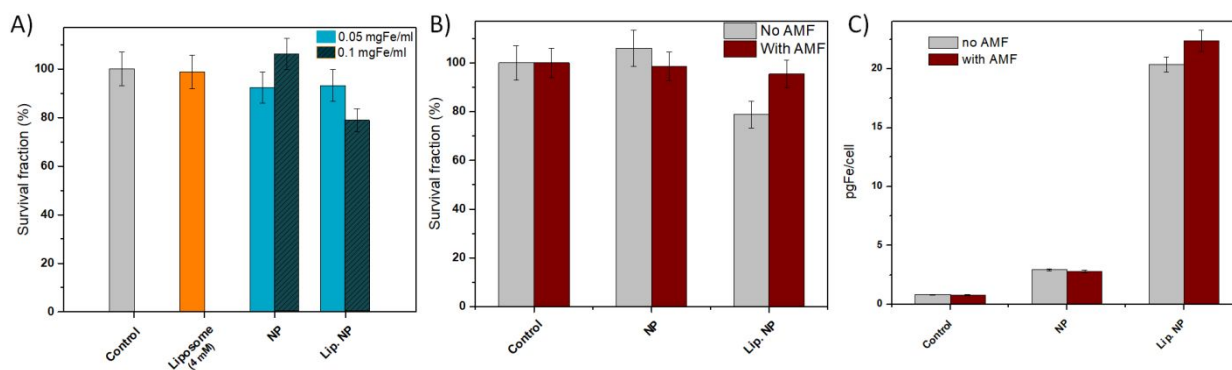


Figure 6. Toxicity evaluation by MTT assay with MDA-MB-231 cells tested with A) 15 nm NP coated by DMSA, bare liposomes and magnetoliposomes at different concentrations. B) MTT assay after the application of an AMF for 1 h (202 kHz + 30 mT). C) Intracellular absorption of the materials measured by ICP and calculated as an estimation of iron per cell.

HeLa cells were also used to test the toxicity of the materials as a complementary result, given their wide use in nanotoxicity evaluations providing a good basis for comparison with bibliographic data⁵⁰⁻⁵⁵ (figure S5). For 0.05 mgFe/ml, cell survival was above 90 % in all cases, while doubling the iron concentration decreased cell survival (figure S5A). As described for MDA-MB-231 cells, magnetic hyperthermia by AMF did not trigger a significant cell death (figure S5B). Figure S6 shows Prussian Blue images highlighting cell internalization of the NP around the nucleus (but never inside), as previously reported,^{54, 56} for different iron concentrations (from 0.05 up to 0.2 mgFe/ml) of DMSA-coated NP of 8 and 15 nm. As also described, the use of magnetoliposomes increased cell labelling efficiency when compared to free NP. Typically, magnetoliposomes are bound to the cell surface after 60 min and after 180 min they were internalized.⁵⁷

DOX was successfully encapsulated in the inner part of the magnetoliposomes during liposome synthesis. DOX release was monitored by spectrophotometry as a function of time, dialysis, temperature and applied magnetic field for 1 h (202 kHz and 30 mT). Initially, an encapsulation efficacy of more than 85 %, corresponding to 43 μ M was achieved in liposomes and magnetoliposomes, similar to previous results.¹² After just one-hour post-synthesis 20 % was released in both cases, which will not change even after 48 h, suggesting that the drug is in equilibrium with the medium. However, the release increased up to 95 % after 48 h dialysis due to the DOX molecules freely diffusing across the membrane (similar results have been reported over 24 h⁵⁸). The lipid bilayer is not totally rigid due to lack of cholesterol in the mixture.⁴⁸ Finally,

applying an alternate magnetic field of 202 kHz (30 mT) for 1 hour produces an extra release of 27 % of DOX only for magnetoliposomes. The same result is obtained if the magnetoliposomes are maintained at 45 °C in a bath for 1 hour. No further release was observed after 24 h once the applied field was switched off nor after removing the hot bath. This suggests that the transition temperature of the bilayer has been achieved by the application of the magnetic field and by the bath. Similar results have been already published for magnetoliposomes containing DOX, with a passive release of 5-20 % that goes up to 60 % after AMF application.^{12, 46, 58-62} DOX is not the only cargo that can be encapsulated, but also magnetoliposomes with NP embedded in the membrane, loaded with calcein presented a 25 % release after AMF application for 2 h.⁶³

MDA-MB-231 cell cultures were then exposed to magnetoliposomes loaded with DOX. The excess NP/liposomes were removed after 24 hours, so only the ones either internalized or attached to the cell surface remained in the culture. FESEM images showed NP agglomerations in direct contact with the cell membranes (figure S7A). However, magnetoliposomes were more difficult to identify (figure S7B, C) due to their organic composition and their hypothesized localization in the inner part of the cells instead of their surface (as happened with free NP).

The viability of MDA-MB-231 cells exposed to the different material treatments, including the applications of an AMF, was then analyzed by calcein/EthD-1 staining and confocal laser scanning microscopy (figure 7 and Table S1). Bright field images are included in SI for morphological appreciation of the cultures (figure S8). It should be noted that MDA-MB-231 is an adherent cell line, which means that dead cells detach and float in the culture media, being washed away during culture media replacement. Iron and DOX concentrations were fixed in the study. However, lipids concentration was difficult to maintain unchanged, making survival with liposomes as low as 50 % due to toxicity associated to their concentrations and degradations time. Free DOX at 0.4 μM concentration caused a huge drop of survival, representing less than 3 % respect to the control, as previously reported.³⁴ Importantly, when DOX was encapsulated in liposomes, a huge increase in cell survival up to 72 % was found, meaning that liposomes were able to slow down DOX diffusion. The treatment with 15 nm magnetic NP and magnetoliposomes produced a normalized survival of 82 % and 115 %, respectively. Finally, the use of magnetoliposomes as a carrier for DOX increased cell survival to 88 %, confirming the efficiency of magnetoliposomes to protect DOX from undesired release and, therefore, cells from DOX toxic effects before deployment, partially reverting doxorubicin toxicity by interfering with the passive release of the drug. The fact that the nanoparticles locate at the periphery of the liposome supports this hypothesis of interference.

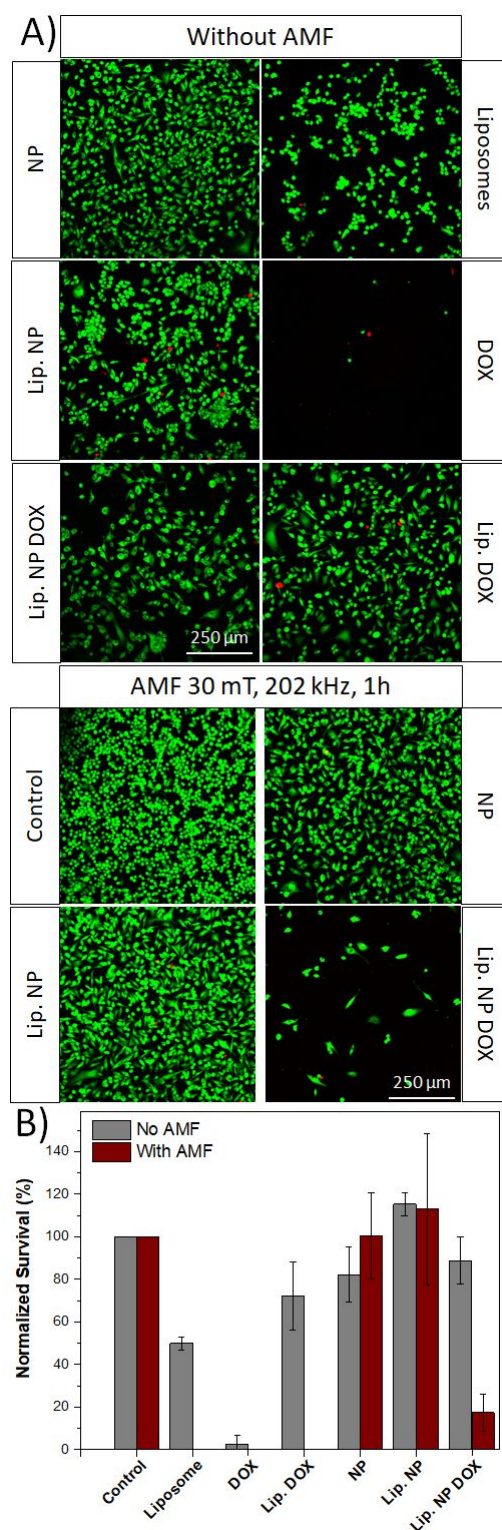


Figure 7. Viability studies of MDA-MB-231 cells after exposure to different treatments. Concentrations of 0.1 mgFe/ml and 0.4 μ M DOX were kept constant. A) Representative images by confocal laser scanning microscopy where live cells appear in green and dead cells appear in red. B) Normalized survival after 24h of exposure to different treatments without (gray bars) and with AMF of 202 kHz and 30 mT for 1 h (red bars).

Finally, an AMF was applied to the cell cultures containing DOX-loaded magnetoliposomes to verify the capacity of the field to trigger DOX release. MDA-MB-231 cells were placed in a coil, with the configuration of 202 kHz and 30 mT (24 kAm^{-1}), configuration that gave the best SAR values for 15 nm core NP figure 3A. First, we confirmed that cell survival was preserved (100 %) when cells loaded with NP were exposed to the AMF for 1 h. Importantly, survival of the cells loaded with magnetoliposomes reached a value of 112 %, so confirming no evident cell death caused by magnetic hyperthermia (in agreement with results from MTT tests, figure 6B). The combination of magnetoliposomes with DOX and AMF reduced cell survival to 17 % (a 70 % reduction after applying the AMF). It is worth to note that, although similar results were reported for comparable DOX-loaded magnetoliposomes, much higher magnetic field frequencies were needed.³⁴ Cell death increased when extending the duration of AMF (from 5 min up to 1 h). Alternatively, conventional hyperthermia (water bath at 46 °C for 30 min) reached cell death percentages of less than 10 %.⁶⁴

One last parameter that should draw attention and taken into account is the local effect of the AMF, determinant for the treatment of a specific area/tumor. It was observed that cell survival only diminished in the areas closer to the center of the field (10 % of survival), where the magnitude of the AMF was maximum), while increased in further areas (closer to the borders) (Figure 8). This localized effect is a crucial advantage of this treatment for future applications *in-vivo* that allow avoiding damage to the surrounding healthy tissues.

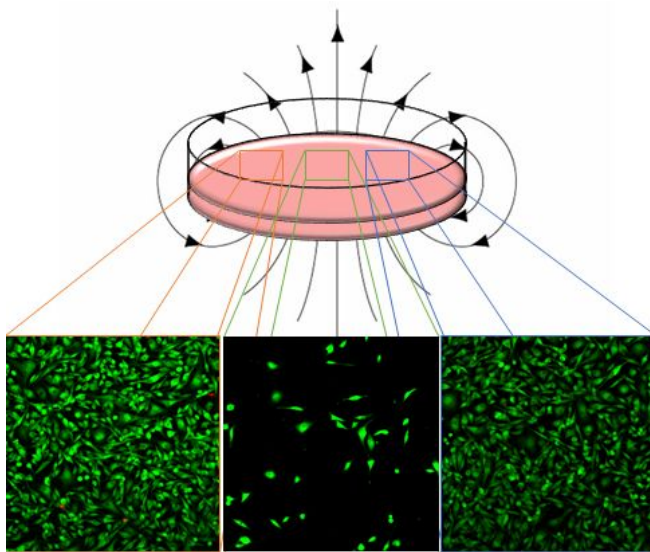


Figure 8. Distance effect on the viability of MDA-MB-231 cells carrying DOX-loaded magnetoliposomes after exposure to an AMF for 1 h, depending on the location in the plate. As observed, cell survival dramatically decreased in the center of the magnetic field and increased towards the borders of the plate. Live cells appear in green while dead cells in red.

CONCLUSIONS

Magnetoliposomes of around 200 nm containing 15 nm DMSA-coated magnetic NP attached outside the lipid surface and DOX encapsulated inside have the ideal colloidal, magnetic and heating properties to be used as a drug delivery system with remote control of the drug release by applying an AMF.

We demonstrated that it is possible to control the spatial distribution of the NP in the liposome by controlling the nanoparticle surface charge and indispensable tools such as Cryo-TEM and AFM have been used for the characterization of these colloidal drug delivery systems. The membrane integrity of the liposomes is preserved for concentrations of around 15 NP/liposome although there is a certain perturbation of the bilayer due to the presence of the particles. Thus, the melt transition temperature of the lipid bilayer shifts from 41.6 °C down to around 38.7 °C with a slight reduction in enthalpy from 38.6 J/g to 34.8 J/g, allowing the encapsulation of DOX and slowing down its release.

Although the heating efficiency of the NP is reduced when they are immobilized at the liposome surface, SAR values for these magnetoliposomes are still around 100 W/g Fe at 202 kHz + 30 mT (patient tolerated conditions), which seems to be enough to overcome the lipid melt transition temperature reaching the drug release on demand. Heat performance of the particles have been largely improved by the synthesis method that allows better control over NP structural properties. Drug release control using an AMF was adjusted for MDA-MB-231, triple-negative breast cancer cells. Applying an AMF for 1 h, drug release was triggered reaching a cell death rate as high as 83 %. The local heat transfer of the NP to the lipid region surrounding the NP surface is fast and very efficient. Without AMF, these magnetoliposomes accumulate in the cell cytoplasm reaching a 100 % labelling efficiency and maintaining cell viability above 80 %.

Future work will focus on the use of multi-drugs in a combinatorial drug therapy, taking advantage of the hydrophobic area between the lipid bilayers to encapsulate hydrophobic drugs such as photodynamic ones.⁶⁵ Moreover, by adjusting AMF conditions, mechanical damage can also be induced to the magnetic NP providing an additional tool to eliminate fat deposits and blood clots. These relatively big magnetic NP also provide changes in the MRI T₂ contrast that could be used to follow the magnetoliposomes circulation and accumulation and, finally, to predict when the AMF should be applied to enhance the synergic effects in a more accurate way.

MATERIALS AND METHODS

Liposomes were prepared by a thin-layer evaporation method⁶⁶ using 1,2-Dipalmitoyl-sn-glycero-3-phosphocholine (DPPC). Lipids (5 mg) were dissolved in 5 mL of chloroform, inside a round bottom glass flask of 50 ml for 20 minutes. The solvent was removed by rotary evaporation for 1 h under vacuum at 60 °C. Then, the dried lipid film was hydrated with 5 mL of distilled water at 55 °C. The product of this hydration is a large multilamellar vesicle (LMV). To break these

structures, it is necessary to sonicate the mixture at 55 °C for 1 h producing small unilamellar vesicles (SUV), with diameters up to 200 nm (the presence of some LMV cannot be discarded).⁶⁷ The dispersion was then placed in a cellulose membrane tube MWCO 10000 Da and dialyzed for 2 days in distilled water. Finally, the pH of the dispersion was adjusted to 7, and the dispersion was filtered through a polyethylene oxide filter with a pore size of 0.45 μm .

Magnetic nanoparticles synthesis was carried out by thermal decomposition of an organic precursor in organic media in the presence of oleic acid following procedures found in literature but using standardized protocols.⁶⁸ In brief, a mixture containing 0.9 g of solid iron oleate, 4.5 g of oleic acid, and 50 ml of octadecene was added on a three-neck round bottom flask mounted on a temperature-controlled N_2 reflux system, overhead stirred at 100 rpm until reaching 100 °C. The temperature was increased in a controlled way, with a heating ramp of 3.75 °C/min until reflux temperature, given by boiling point of the solvent (320 °C), and this temperature was maintained for 1 h. After washing with ethanol, 15 nm nanoparticles coated with oleic acid were obtained. Those nanoparticles were transferred to water by exchanging the oleic acid at the surface by dimercaptosuccinic acid (DMSA).⁶⁹ For comparison, smaller nanoparticles with the same coating (DMSA) and particles with similar size but positively coated with 3-Aminopropyltriethoxysilane (APS) were used and the synthesis procedures are described in the supporting information.

To produce magnetoliposomes with hydrophilic nanoparticles (coated with either DMSA or APS) the process is analogous to the liposomes, where 5 mg of the nanoparticles are dispersed in 5 mL of distilled water, used to hydrate the dried lipid film. To produce magnetoliposomes with hydrophobic nanoparticles (coated with oleic acid), 5 mg of nanoparticles are dispersed in 5 mL of chloroform at the beginning of the process. To synthesize liposomes loaded with DOX 2.5 mL of doxorubicin hydrochloride 98 % (100 μM) were added to 2.5 mL of distilled water, used to hydrate the dried lipid film. As DOX is photosensitive, the processes of synthesis have to be made in the dark (with everything covered by aluminum foil). Also, commercial liposomes produced by NanoVex Biotechnologies S.L. (LipoCat) were tested for comparison. These cationic liposomes are formed by adding water to the lipid powder provided in sealed vials by hand shaking. In this case the hydrophilic nanoparticles (5 mg) were added with 5 mL distilled water and posterior sonication of the mixture at 55 °C.

The core size and shape of nanoparticles and magnetoliposomes were measured by transmission electron microscopy (TEM), where a drop of the dispersion was placed on a copper grid coated with perforated carbon film, allowing all the solvent to evaporate at room temperature. In the particular case of magnetoliposomes a drop of the suspension was placed on a carbon coated copper grid removing the excess by filter paper. To stain the liposomes, a drop of 2 % (w/v) aqueous solution of uranyl acetate was added and left in contact with the sample for 2 minutes. The surplus water was removed and the grid was dried at room conditions. Size distribution were obtained with the open source software ImageJ, counting at least 300 nanoparticles [ISO13322-1].

Cryo-TEM was used to observe frozen hydrated liposomes with intact morphology.⁷⁰ The sample was applied to QUANTIFOIL[®] holey carbon grid (Cu/Rh R 3.5/1), which is a perforated support carbon foil with circular holes and after a soft blotting, frozen extremely rapidly, at a rate of 10^6 °C/s, so that the water inside and surrounding the liposome was fixed in a vitreous state. A FEI Vitrobot (ThermoFisher Scientific[®]) was used to prepare the grids incubated at 22 °C and 95 % humidity. Inside the Vitrobot equipment, a drop of 3 μ l of sample at 0.05 mg DPPC/ml concentration was put in contact with the grid for 15 seconds. The grid was blotted using filter paper for 3 seconds, which is then immersed into the liquid ethane, cooled at -180 °C by liquid nitrogen. After immersion, the grid must be kept under liquid nitrogen until its use. To acquire the images, it was used EPU Software (ThermoFisher Scientific[®]) for automation of the process installed on a 200 kV Talos Arctica equipped with a Falcon III Direct Detector Device.

The atomic force microscopy experiments were performed with commercial AFM (Cypher, Asylum Research) operated in a bimodal AM open loop configuration.⁴³ The diluted samples were deposited on freshly cleaved mica and measured in Milli-Q water at room temperature. The images were obtained with a microcantilever BL-AC40TS (Olympus, Japan) characterized by $f_1 = 28$ kHz, $k_1 = 0.052$ N m⁻¹, $Q_1 = 1.5$ (measured in water), $f_2 = 228$ kHz, $k_2 = 3.4$ N m⁻¹ and $R = 2$ nm (nominal radius). Bimodal AFM was performed by driving the microcantilever first and second resonances with amplitudes $A_{01} = 12.0$ nm, $A_1 = 9.6$ nm and $A_2 = 0.8$ nm. Amplitude modulation AFM was performed with the same type of cantilever ($A_{01} = 2.0$ nm, $A_1 = 1.8$ nm). Here, the bimodal AFM compositional contrast measures how mechanical energy from the AFM tip is dissipated into the liposome, NP and lipid bilayer.

Fourier transform infrared spectroscopy (FTIR) spectra were recorded using a Bruker IFS 66VS between 4000 and 250 cm⁻¹ and the samples were prepared by diluting 2 % wt iron oxide powder in KBr and pressing it into a pellet. Iron determination was carried out by Inductively Coupled Plasma–Optical Emission Spectrometry (ICP-OES) using an instrument from PerkinElmer, OPTIMA 2100DV model, with prior digestion of the nanoparticles and liposomes using nitric acid at 90 °C for at least 4 hours.

To evaluate the phase transition temperatures of the liposomes it was used a differential scanning calorimeter (DSC) MicroCal VP-DSC (MicroCal LLC, Northampton, MA, USA) with a cell volume of 0.514 ml, where the reference cell is filled with distilled water. The heat flow between cells has been explored with a temperature increase rate of 1 °C per minute, and the temperature range covered was from 15 °C to 75 °C. The hydrodynamic particle size of the samples at pH 7 was measured by dynamic light scattering (DLS) in a standard cuvette, using a Zetasizer NanoZS device (Malvern Instruments), and the refraction index used was 2.42. The intensity data were analyzed to obtain the intensity, volume, and number distributions. The zeta potential was measured for the nanoparticles and magnetoliposomes at pH 7, with distilled water at room temperature, using 0.01 M KNO₃ as background electrolyte.

Frequency dependence of the AC magnetic susceptibility (ACS) was measured using two AC susceptometers. DynoMag system was utilized between 1 Hz and 500 kHz, then a high frequency AC susceptometer was used in the frequency range between 500 kHz and 10 MHz. Measurements were carried out at room temperature with the samples in liquid (200 mL), using excitation fields in the range of 30 mT to 500 mT. AC susceptibility spectra were recorded as a function of the frequency, and the curves were fitted to obtain the hydrodynamic size using different models. Data were normalized such that the maximum χ' values (at low frequencies) were unity in each case, for comparison. Fit models can be seen in supporting information at the 'used models for ac susceptibility' section.

Specific power absorption rate (SAR) was measured on a Fives Celes generator specially designed for heating magnetic nanoparticles model N° 12118 M01 (France), equipped with water cooled electrolytic copper made 50 mm diameter coils with 6 numbers of turns. The sample was kept in a vial and placed at the center of the heating coil. Experiments were performed under frequencies of 92, 202 or 282 kHz at different external field amplitudes, 52, 24 or 17 kAm⁻¹ respectively. Sample temperature was measured using a fiber optic temperature sensor (OSENSA's FTX). SAR was determined from the ΔT vs time curves (where ΔT indicates temperature increase over the base line temperature), $SAR = C_p (m_s/m_F) * (\Delta T/\Delta t)$, where C_p is the solution specific heat (4.18 J/g°C for water), m_s the total ensemble mass, m_F the magnetite mass and $\Delta T/\Delta t$ the initial slope of the field induced heating curve. As the measurements are performed in nonadiabatic conditions, the curve slope is fitted only in the first few seconds after turning the magnetic field on, typically during the first 30 s. Measurements were done with at least 500 μ l, and sample was sonicated for 5 minutes before to prevent precipitation. In this work the initial temperature was settled at 37.2 °C with a refrigerator.

Drug release experiments were carried out with DOX taking advantage of its optical properties. A Biochorom WPA Biowave DNA UV-Visible spectrophotometer was used over the wavelength range from 450 to 700 nm. The samples were dispersed in water and placed on a 1 mm wide quartz cuvette. The spectral range of the apparatus is 190-900 nm (5 nm bandwidth). The precision of the equipment is ± 2 nm. A standard curve was recorded with concentrations from 1 to 100 μ M of DOX. For the experiments *in-vitro*, an initial concentration of 50 μ M was used. The DOX release from liposomes was evaluated as a function of time up to 48 h, as a function of temperature up to 45 °C for one hour, as a function of applied magnetic field with 30 mT for one hour and finally as a function of dialysis up to 48 h.

In-vitro experiments were performed by using two different cancer cells lines: MDA-MB-231 and HeLa cells. MDA-MB-231 cells (a human breast cancer cell line) were cultured in Dulbecco's Modified Eagle's Medium (DMEM) supplemented with 10 % fetal bovine serum (FBS), 100 mg/ml streptomycin, 100 U/ml penicillin, and 1 mM L-glutamine in standard culture conditions (37 °C, 5 % CO₂, 90 % relative humidity). These cells were seeded at a density of 25 x 10³ cells per well in a 24-well plate and 125 x 10³ cells per petri plate (35 mm) (subconfluence conditions).

Three days after cell seeding, cultures were exposed to different treatments by adding them to the cell culture medium. Treatments consisted on: free DOX, liposomes, NP, DOX-loaded liposomes, magnetoliposomes and DOX-loaded magnetoliposomes. In all cases, concentrations of 0.1 mgFe/ml and 0.4 μ M DOX were maintained, with the suspension being previously sonicated for 5 min before application. After 24 h of exposure, the excess was discarded and culture media was replaced. At this time point, individual petri plates were also subjected to an AMF of 30 mT, 202 kHz for 1 h. Cells were then analyzed after 24 h. HeLa cells (a human cervical cancer cell line) were cultured in DMEM, supplemented with 10 % FBS, 50 U/ml penicillin and 50 mg/mL streptomycin. Cells were seeded at a density of 25×10^3 per well in 24-well plates and 75×10^3 cells in individual petri plates (35 mm diameter). Cell cultures were then incubated for 24 h at 37 °C with different concentrations of nanoparticles (0.05 and 0.1 mgFe/ml). In all cases, control cells were cultured onto glass coverslips following the same protocol described above for comparison.

Cell culture morphology was observed under an AE2000 optical inverted microscope (Motic) and a fluorescence microscope Leica DMI6000B equipped with an OrcaR2 monochrome digital camera. Specific details of nanoparticles and magnetoliposomes interaction with the cell surface were observed by scanning electron microscopy (SEM) and field emission scanning electron microscopy (FESEM). Specifically, cells were fixed with glutaraldehyde (4 % in phosphate buffer saline, PBS) for 45 min. Samples were then washed twice in distilled water and underwent a serial dehydration with increasing ethanol concentration solutions (two washes of 15 min each), until a final treatment with absolute ethanol for 30 min. Samples were allowed to dry for at least 48h. Finally, they were mounted in stubs and coated either with gold (10 nm for SEM studies) or with chromium (15 nm for FESEM studies) under vacuum conditions. Samples were observed by using a Hitachi S-3000N scanning electron microscope (SEM), and a Philips XL30 S-FEG field emission scanning electron microscope (FESEM).

Cellular uptake of the nanoparticles, expressed as the amount of iron per cell, was estimated from iron measurements by elemental analysis using ICP-OES analysis. Cell digestion was carried out at 90 °C, using 900 mL of 65 % (v/v) HNO_3 (1 h) and then 1 mL of 30 % (p/v) H_2O_2 and then diluted with distilled water up to 10 mL. Untreated cells were also analyzed to subtract the amount of endogenous iron. Data obtained by the elemental analysis were normalized by the number of cells per sample, previously counted using a Neubauer chamber.

To localize and visualize the intracellular nanoparticles distribution Prussian blue staining was performed to detect iron. Cell culture samples were fixed in paraformaldehyde (PFA) 4 % for 12 min and washed twice with distilled water. Then, they were treated with methanol at 20 °C for 5 min and allowed to dry for 2 h. Cultures were then stained for 15 min with a solution of 2 % potassium ferrocyanide and 2 % HCl in distilled water. After two washes in distilled water, cells were counterstained with 0.1 % neutral red in distilled water for 2 min and washed in distilled water to remove the excess dye. Images were collected by using an Olympus BX61 microscope.

Cytotoxicity assays on MDA-MB-231 cells were performed by using a Live-Dead kit according to the manufacturer's instructions (Life Sciences). This kit is based on the use of calcein and ethidium homodimer-1 (EthD-1). Calcein is a non-fluorescent cell permeable dye that gets converted into a strong green light emitting compound after contact with intracellular esterases and so retained inside live cells. In contrast, EthD-1 is a DNA intercalating agent that penetrates cell membranes in dead cells and emits red fluorescence when inserted into the DNA double helix. In this work, samples were incubated with a solution containing calcein (2 μ M) and EthD-1 (4 μ M) in PBS during 10 min at 37 °C, in a 5 % CO₂ atmosphere. After staining, samples were visualized by using a fluorescence microscope Leica DMI6000B equipped with an OrcaR2 monochrome digital camera. The fluorescence of both probes was excited by an argon laser tuned to 488 nm. After excitation, emitted fluorescence was separated by using a triple dichroic filter 488-561-633 and measured in the range 505-570 nm for green fluorescence (calcein) and 630-750 nm for red fluorescence (EthD-1). Immunofluorescence images of both living and dead cells were analyzed by using the Fiji software, where the number of pixels positive for either green or red fluorescences were quantified in square micrometers (μ m²) and finally expressed as a total percentage of the total image area. Mitochondrial activity of MDA-MB-231 and HeLa cells were assessed by the MTT colorimetric assay. Cells exposed to treatments were incubated with a 0.5 mg/mL solution of dimethylthiazolyl-diphenyl-tetrazolium bromide (MTT, Sigma-Aldrich) in DMEM. Cells were incubated for 3 h (37 °C, 5 % CO₂) until the formation of formazan precipitates, which were then dissolved with isopropanol/HCL (0.04 N) for 90 min. Finally, absorbance was measured at 570 nm in a SpectraFluor spectrophotometer (Tecan Group Ltd, Mannedorf, Switzerland). Mitochondrial activity, as an indirect indicator of cell survival, was expressed as the percentage of absorption of treated cells in comparison with that of control cells without treatment.

For cell proliferation experiments, cell cultures were washed with PBS at 37 °C and incubated with trypsin (5 min, 37 °C, 5 % CO₂). Trypsin was then inactivated by adding DMEM supplemented with FBS. Finally, sample volumes were collected in eppendorf tubes and cells counted by using a Neubauer chamber under an AE2000 optical inverted microscope (Motic).

ASSOCIATED CONTENT

Supporting Information. Fit models for ac susceptibility, TEM images of the nanoparticles, liposomes and magnetoliposomes at different magnifications. Nanotoxicity tests for HeLa cell lines with Prussian blue reaction.

AUTHOR INFORMATION

Corresponding Author

* brollo@icmm.csic.es

* puerto@icmm.csic.es

Author Contributions

The manuscript was written through contributions of all authors. All authors have given approval to the final version of the manuscript.

ACKNOWLEDGMENT

M. E. F. Brollo acknowledges the Brazilian agency CNPq for the grant [232947/2014-7] within the Science without Borders program and the COST action program for the grant [TD1402 – 38989]. The work was supported by the Spanish Government under projects MAT2017-88148-R (AEI/FEDER, UE), MAT2016-78857-R (AEI/FEDER, UE), MAT2016-76507-R, CTQ2016-78454-C2-2-R, by the Comunidad de Madrid (S2018/NMT-4321 NANOMAGCOST-CM), the European Research Council through ERC-AG grant 340177. IMDEA Nanociencia acknowledges support from the ‘Severo Ochoa’ Programme for Centres of Excellence in R&D (MINECO, Grant SEV-2016-0686). The characterization was performed using the ICMM/CSIC general services (X-ray, ICP). ACS analyses were performed at RISE Acreo in Gothenburg, Sweden and cryo-TEM images were taken by Dr. Francisco Javier Chichón at the Cryo-EM facility (CiB-CNB-CSIC) placed on the National Center for Biotechnology in Madrid, Spain.

REFERENCES

1. Bulbake, U.; Doppalapudi, S.; Kommineni, N.; Khan, W., Liposomal Formulations in Clinical Use: An Updated Review. *Pharmaceutics* **2017**, 9 (2), 12.
2. Bobo, D.; Robinson, K. J.; Islam, J.; Thurecht, K. J.; Corrie, S. R., Nanoparticle-Based Medicines: A Review of FDA-Approved Materials and Clinical Trials to Date. *Pharm. Res.* **2016**, 33 (10), 2373-2387.

3. Cagel, M.; Grotz, E.; Bernabeu, E.; Moretton, M. A.; Chiappetta, D. A., Doxorubicin: Nanotechnological Overviews from Bench to Bedside. *Drug Discovery Today* **2017**, 22 (2), 270-281.
4. Aiken, M. J.; Suhag, V.; Garcia, C. A.; Acio, E.; Moreau, S.; Priebat, D. A.; Chennupati, S. P.; Nostrand, D. V., Doxorubicin-Induced Cardiac Toxicity and Cardiac Rest Gated Blood Pool Imaging. *Clin. Nucl. Med.* **2009**, 34 (11), 762-767.
5. Hoff, D. D. V.; Layard, M. W.; Basa, P.; Hugh L Davis, J.; Hoff, A. L. V.; Rozenzweig, M.; Muggia, F. M., Risk Factors for Doxorubicin-Induced Congestive Heart Failure. *Ann. Intern. Med.* **1979**, 91, 710-717.
6. Ulbrich, K.; Holá, K.; Šubr, V.; Bakandritsos, A.; Tuček, J.; Zbořil, R., Targeted Drug Delivery with Polymers and Magnetic Nanoparticles: Covalent and Noncovalent Approaches, Release Control, and Clinical Studies. *Chem. Rev.* **2016**, 116 (9), 5338-5431.
7. Guo, S.; Li, D.; Zhang, L.; Li, J.; Wang, E., Monodisperse Mesoporous Superparamagnetic Single-crystal Magnetite Nanoparticles for Drug Delivery. *Biomaterials* **2009**, 30 (10), 1881-1889.
8. Golovin, Y. I.; Gribovsky, S. L.; Golovin, D. Y.; Klyachko, N. L.; Majouga, A. G.; Master, A. M.; Sokolsky, M.; Kabanov, A. V., Towards Nanomedicines of the Future: Remote Magneto-Mechanical Actuation of Nanomedicines by Alternating Magnetic Fields. *J. Controlled Release* **2015**, 219, 43-60.
9. Preiss, M. R.; Bothun, G. D., Stimuli-Responsive Liposome-Nanoparticle Assemblies. *Expert opin. drug delivery* **2011**, 8 (8), 1025-1040.
10. Shaghasemi, B. S.; Virk, M. M.; Reimhult, E., Optimization of Magneto-thermally Controlled Release Kinetics by Tuning of Magnetoliposome Composition and Structure. *Sci. Rep.* **2017**, 7 (7474), 10.
11. Ju, L.; Cailin, F.; Wenlan, W.; Pinghua, Y.; Jiayu, G.; Junbo, L., Preparation and Properties Evaluation of a Novel pH-Sensitive Liposomes Based on Imidazole-Modified Cholesterol Derivatives. *Int. J. Pharm.* **2017**, 518 (1), 213-219.
12. Pradhan, P.; Giri, J.; Rieken, F.; Koch, C.; Mykhaylyk, O.; Döblinger, M.; Banerjee, R.; Bahadur, D.; Plank, C., Targeted temperature sensitive magnetic liposomes for thermo-chemotherapy. *J. Controlled Release* **2010**, 142 (1), 108-121.
13. Reimhult, E., Nanoparticle-Triggered Release from Lipid Membrane Vesicles. *New Biotechnol.* **2015**, 32 (6), 665-672.
14. Soenen, S. J. H.; Hodenius, M.; De Cuyper, M., Magnetoliposomes: Versatile Innovative Nanocolloids for Use in Biotechnology and Biomedicine. *Nanomedicine* **2009**, 4 (2), 177-191.
15. Mai, B. T.; Fernandes, S.; Balakrishnan, P. B.; Pellegrino, T., Nanosystems Based on Magnetic Nanoparticles and Thermo- or pH-Responsive Polymers: An Update and Future Perspectives. *Acc. Chem. Res.* **2018**, 51 (5), 999-1013.
16. Li, Q.; Li, W.; Di, H.; Luo, L.; Zhu, C.; Yang, J.; Yin, X.; Yin, H.; Gao, J.; Du, Y.; You, J., A Photosensitive Liposome with NIR Light Triggered Doxorubicin Release as a Combined Photodynamic-Chemo Therapy System. *J. Controlled Release* **2018**, 277, 114-125.
17. Pankhurst, Q. A.; Connolly, J.; Jones, S. K.; Dobson, J., Applications of Magnetic Nanoparticles in Biomedicine. *J. Phys. D: Appl. Phys.* **2003**, 36 (13), R167-R181.
18. Revia, R. A.; Zhang, M., Magnetite Nanoparticles for Cancer Diagnosis, Treatment, and Treatment Monitoring: Recent Advances. *Mater. Today (Kidlington)* **2016**, 19 (3), 157-168.
19. Dong, J.; Zink, J. I., Taking the Temperature of the Interiors of Magnetically Heated Nanoparticles. *ACS Nano* **2014**, 8 (5), 5199-5207.

20. Gonzalez-Angulo, A. M.; Morales-Vasquez, F.; Hortobagyi, G. N., Overview of Resistance to Systemic Therapy in Patients with Breast Cancer. In *Breast Cancer Chemosensitivity*, Yu, D.; Hung, M.-C., Eds. Springer New York: New York, NY, 2007; pp 1-22.
21. Miller-Kleinhenz, J. M.; Bozeman, E. N.; Yang, L., Targeted Nanoparticles for Image-Guided Treatment of Triple-Negative Breast Cancer: Clinical Significance and Technological Advances. *Wiley Interdiscip. Rev.: Nanomed. Nanobiotechnol.* **2015**, 7 (6), 797-816.
22. Morini, M. A.; Sierra, M. B.; Pedroni, V. I.; Alarcon, L. M.; Appignanesi, G. A.; Disalvo, E. A., Influence of Temperature, Anions and Size Distribution on the Zeta Potential of DMPC, DPPC and DMPE Lipid Vesicles. *Colloids Surf., B* **2015**, 131, 54-58.
23. Inoue, T.; Yanagihara, S.-i.; Misono, Y.; Suzuki, M., Effect of Fatty Acids on Phase Behavior of Hydrated Dipalmitoylphosphatidylcholine Bilayer: Saturated Versus Unsaturated Fatty Acids. *Chem. Phys. Lipids* **2001**, 109 (2), 117-133.
24. Park, S.-H.; Oh, S.-G.; Mun, J.-Y.; Han, S.-S., Effects of Silver Nanoparticles on the Fluidity of Bilayer in Phospholipid Liposome. *Colloids Surf., B* **2005**, 44 (2-3), 117-122.
25. Park, S.-H.; Oh, S.-G.; Mun, J.-Y.; Han, S.-S., Loading of Gold Nanoparticles Inside the DPPC Bilayers of Liposome and their Effects on Membrane Fluidities. *Colloids Surf., B* **2006**, 48 (2), 112-118.
26. Bothun, G. D., Hydrophobic Silver Nanoparticles Trapped in Lipid Bilayers: Size Distribution, Bilayer Phase Behavior, and Optical Properties. *J. Nanobiotechnol.* **2008**, 6 (1), 13.
27. Gillot, B.; Jemali, F., Infrared Studies on the Behavior in Oxygen of Cobalt-Substituted Magnetites: Comparison with Zinc-Substituted magnetites. *J. Solid State Chem.* **1983**, 50, 138-145.
28. Abenojar, E. C.; Wickramasinghe, S.; Bas-Concepcion, J.; Samia, A. C. S., Structural Effects on the Magnetic Hyperthermia Properties of Iron Oxide Nanoparticles. *Prog. Nat. Sci.: Mater. Int.* **2016**, 26 (5), 440-448.
29. Yoo, D.; Lee, J.-H.; Shin, T.-H.; Cheon, J., Theranostic Magnetic Nanoparticles. *Acc. Chem. Res.* **2011**, 44 (10), 863-874.
30. Fortin, J.-P.; Wilhelm, C.; Servais, J.; Ménager, C.; Bacri, J.-C.; Gazeau, F., Size-Sorted Anionic Iron Oxide Nanomagnets as Colloidal Mediators for Magnetic Hyperthermia. *J. Am. Chem. Soc.* **2007**, 129 (9), 2628-2635.
31. Sonvico, F.; Mornet, S.; Vasseur, S.; Dubernet, C.; Jaillard, D.; Degrouard, J.; Hoebeke, J.; Duguet, E.; Colombo, P.; Couvreur, P., Folate-Conjugated Iron Oxide Nanoparticles for Solid Tumor Targeting as Potential Specific Magnetic Hyperthermia Mediators: Synthesis, Physicochemical Characterization, and in Vitro Experiments. *Bioconjugate Chem.* **2005**, 16 (5), 1181-1188.
32. Müller, R.; Hergt, R.; Zeisberger, M.; Gawalek, W., Preparation of Magnetic Nanoparticles with Large Specific Loss Power for Heating Applications. *J. Magn. Magn. Mater.* **2005**, 289, 13-16.
33. Jordan, A.; Scholz, R.; Wust, P.; Schirra, H.; Thomas, S.; Schmidt, H.; Felix, R., Endocytosis of Dextran and Silan-Coated Magnetite Nanoparticles and the Effect of Intracellular Hyperthermia on Human Mammary Carcinoma Cells In-Vitro. *J. Magn. Magn. Mater.* **1999**, 194 (1), 185-196.
34. Kossatz, S.; Grandke, J.; Couleaud, P.; Latorre, A.; Aires, A.; Crosbie-Staunton, K.; Ludwig, R.; Dähling, H.; Ettelt, V.; Lazaro-Carrillo, A.; Calero, M.; Sader, M.; Courty, J.; Volkov, Y.; Prina-Mello, A.; Villanueva, A.; Somoza, Á.; Cortajarena, A. L.; Miranda, R.; Hilger, I., Efficient Treatment of Breast Cancer Xenografts with Multifunctionalized Iron Oxide

Nanoparticles Combining Magnetic Hyperthermia and Anti-Cancer Drug Delivery. *Breast Cancer Res.* **2015**, *17* (1), 17.

35. Vreeland, E. C.; Watt, J.; Schober, G. B.; Hance, B. G.; Austin, M. J.; Price, A. D.; Fellows, B. D.; Monson, T. C.; Hudak, N. S.; Maldonado-Camargo, L.; Bohorquez, A. C.; Rinaldi, C.; Huber, D. L., Enhanced Nanoparticle Size Control by Extending LaMer's Mechanism. *Chem. Mater.* **2015**, *27* (17), 6059-6066.

36. Serantes, D.; Simeonidis, K.; Angelakeris, M.; Chubykalo-Fesenko, O.; Marciello, M.; Morales, M. P.; Baldomir, D.; Martinez-Boubeta, C., Multiplying Magnetic Hyperthermia Response by Nanoparticle Assembling. *J. Phys. Chem. C* **2014**, *118* (11), 5927-5934.

37. Béalle, G.; Di Corato, R.; Kolosnjaj-Tabi, J.; Dupuis, V.; Clément, O.; Gazeau, F.; Wilhelm, C.; Ménager, C., Ultra Magnetic Liposomes for MR Imaging, Targeting, and Hyperthermia. *Langmuir* **2012**, *28* (32), 11834-11842.

38. Obaidat, I. M.; Issa, B.; Haik, Y., Magnetic Properties of Magnetic Nanoparticles for Efficient Hyperthermia. *Nanomaterials* **2015**, *5* (1), 63-89.

39. Suto, M.; Hirota, Y.; Mamiya, H.; Fujita, A.; Kasuya, R.; Tohji, K.; Jeyadevan, B., Heat Dissipation Mechanism of Magnetite Nanoparticles in Magnetic Fluid Hyperthermia. *J. Magn. Mater.* **2009**, *321* (10), 1493-1496.

40. Suriyanto; Ng, E. Y. K.; Kumar, S. D., Physical Mechanism and Modeling of Heat Generation and Transfer in Magnetic Fluid Hyperthermia Through Néelian and Brownian Relaxation: a Review. *Biomed. Eng. Online* **2017**, *16* (1), 22.

41. Ahrentorp, F.; Astalan, A.; Blomgren, J.; Jonasson, C.; Wetterskog, E.; Svedlindh, P.; Lak, A.; Ludwig, F.; van Ijzendoorn, L. J.; Westphal, F.; Grüttner, C.; Gehrke, N.; Gustafsson, S.; Olsson, E.; Johansson, C., Effective Particle Magnetic Moment of Multi-Core Particles. *J. Magn. Mater.* **2015**, *380*, 221-226.

42. Gavilán, H.; Kowalski, A.; Heinke, D.; Sugunan, A.; Sommertune, J.; Varón, M.; Bogart, L. K.; Posth, O.; Zeng, L.; González-Alonso, D.; Balceris, C.; Fock, J.; Wetterskog, E.; Frandsen, C.; Gehrke, N.; Grüttner, C.; Fornara, A.; Ludwig, F.; Veintemillas-Verdaguer, S.; Johansson, C.; Morales, M. P., Colloidal Flower-Shaped Iron Oxide Nanoparticles: Synthesis Strategies and Coatings. *Part. Part. Syst. Charact.* **2017**, *34* (7), 12.

43. Rodriguez, T. R.; García, R., Compositional Mapping of Surfaces in Atomic Force Microscopy by Excitation of the Second Normal Mode of the Microcantilever. *Appl. Phys. Lett.* **2004**, *85* (3), 449-451.

44. Perrino, A. P.; Ryu, Y. K.; Amo, C. A.; Morales, M. P.; Garcia, R., Subsurface Imaging of Silicon Nanowire Circuits and Iron Oxide Nanoparticles with Sub-10 nm Spatial Resolution. *Nanotechnol.* **2016**, *27* (27), 275703.

45. Benaglia, S.; Gisbert, V. G.; Perrino, A. P.; Amo, C. A.; Garcia, R., Fast and High-Resolution Mapping of Elastic Properties of Biomolecules and Polymers with Bimodal AFM. *Nat. Protoc.* **2018**, *13* (12), 2890-2907.

46. Joniec, A.; Sek, S.; Krysinski, P., Magnetoliposomes as Potential Carriers of Doxorubicin to Tumours. *Chem.-Eur. J.* **2016**, *22* (49), 17715-17724.

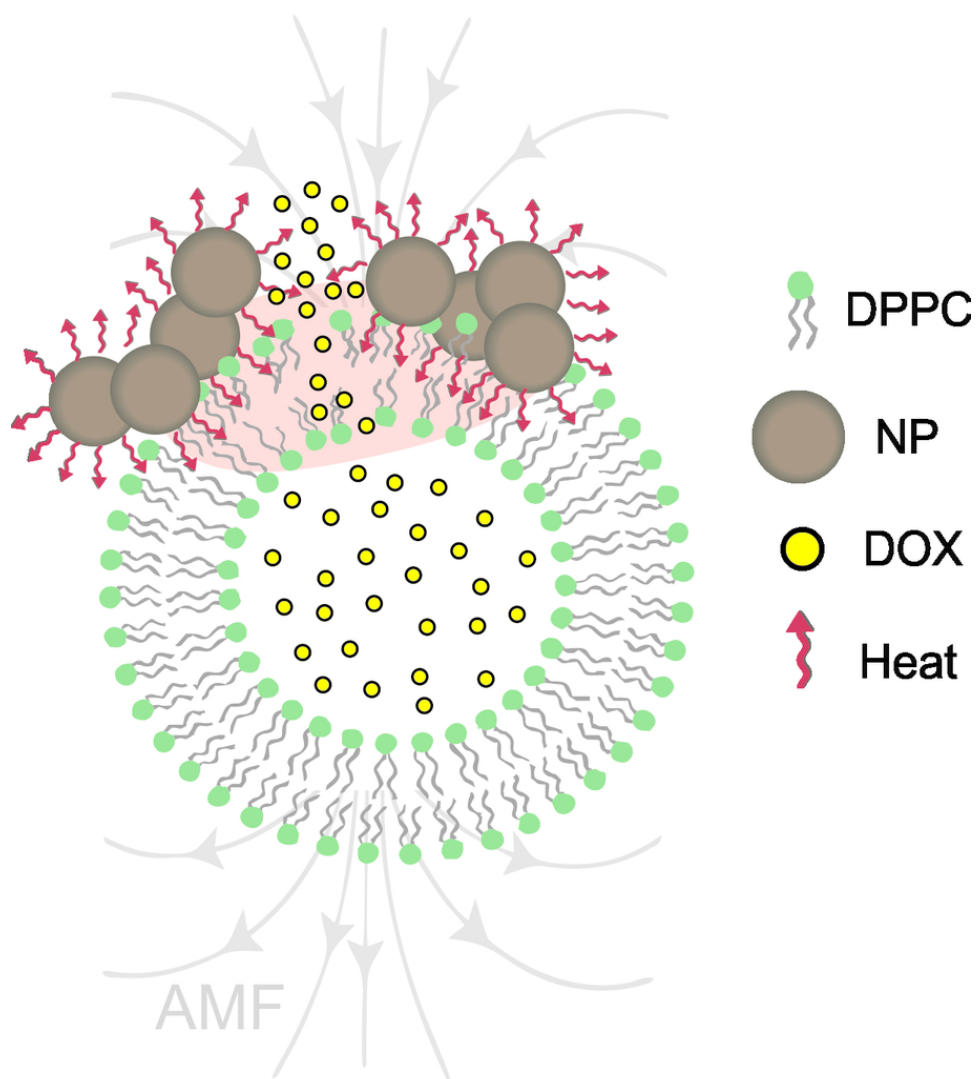
47. Mayhew, E.; Ito, M.; Lazo, R., Toxicity of Non-Drug-Containing Liposomes for Cultured Human Cells. *Exp. Cell Res.* **1987**, *171* (1), 195-202.

48. Lasic, D. D., Mixed Micelles in Drug Delivery. *Nature* **1992**, *355*, 279-280.

49. Nel, A. E.; Mädler, L.; Velegol, D.; Xia, T.; Hoek, E. M. V.; Somasundaran, P.; Klaessig, F.; Castranova, V.; Thompson, M., Understanding Biophysicochemical Interactions at the Nano-Bio Interface. *Nat. Mater.* **2009**, *8*, 543-557.

50. Toro-Cordova, A.; Flores-Cruz, M.; Santoyo-Salazar, J.; Carrillo-Nava, E.; Jurado, R.; Figueroa-Rodriguez, P. A.; Lopez-Sanchez, P.; Medina, L. A.; Garcia-Lopez, P., Liposomes Loaded with Cisplatin and Magnetic Nanoparticles: Physicochemical Characterization, Pharmacokinetics, and In-Vitro Efficacy. *Molecules* **2018**, *23* (9), 2272.
51. Casadó, A.; Mora, M.; Sagristá, M. L.; Rello-Varona, S.; Acedo, P.; Stockert, J. C.; Cañete, M.; Villanueva, A., Improved Selectivity and Cytotoxic Effects of Irinotecan Via Liposomal Delivery: A Comparative Study on Hs68 and HeLa Cells. *Eur. J. Pharm. Sci.* **2017**, *109*, 65-77.
52. Przybylo, M.; Glogocka, D.; Dobrucki, J. W.; Fraczowska, K.; Podbielska, H.; Kopaczynska, M.; Borowik, T.; Langner, M., The Cellular Internalization of Liposome Encapsulated Protoporphyrin IX by HeLa Cells. *Eur. J. Pharm. Sci.* **2016**, *85*, 39-46.
53. Ruiz-González, R.; Milán, P.; Bresolí-Obach, R.; Stockert, J. C.; Villanueva, A.; Cañete, M.; Nonell, S., Photodynamic Synergistic Effect of Pheophorbide a and Doxorubicin in Combined Treatment against Tumoral Cells. *Cancers* **2017**, *9* (2), 18.
54. Villanueva, A.; Cañete, M.; Roca, A. G.; Calero, M.; Veintemillas-Verdaguer, S.; Serna, C. J.; Morales, M. P.; Miranda, R., The Influence of Surface Functionalization on the Enhanced Internalization of Magnetic Nanoparticles in Cancer Cells. *Nanotechnology* **2009**, *20* (11), 115103.
55. Arbab, A. S.; Bashaw, L. A.; Miller, B. R.; Jordan, E. K.; Lewis, B. K.; Kalish, H.; Frank, J. A., Characterization of Biophysical and Metabolic Properties of Cells Labeled with Superparamagnetic Iron Oxide Nanoparticles and Transfection Agent for Cellular MR Imaging. *Radiology* **2003**, *229* (3), 838-846.
56. Calero, M.; Gutierrez, L.; Salas, G.; Luengo, Y.; Lazaro, A.; Acedo, P.; Morales, M. P.; Miranda, R.; Villanueva, A., Efficient and Safe Internalization of Magnetic Iron Oxide Nanoparticles: Two Fundamental Requirements for Biomedical Applications. *Nanomedicine* **2014**, *10* (4), 733-743.
57. Bothun, G. D.; Lelis, A.; Chen, Y.; Scully, K.; Anderson, L. E.; Stoner, M. A., Multicomponent Folate-Targeted Magnetoliposomes: Design, Characterization, and Cellular Uptake. *Nanomedicine (N.Y., NY, U.S.)* **2011**, *7* (6), 797-805.
58. Chen, Y.; Chen, Y.; Xiao, D.; Bose, A.; Deng, R.; Bothun, G. D., Low-Dose Chemotherapy of Hepatocellular Carcinoma Through Triggered-Release from Bilayer-Decorated Magnetoliposomes. *Colloids Surf., B* **2014**, *116*, 452-458.
59. Smondyrev, A. M.; Berkowitz, M. L., Structure of Dipalmitoylphosphatidylcholine/Cholesterol Bilayer at Low and High Cholesterol Concentrations: Molecular Dynamics Simulation. *Biophys. J.* **1999**, *77* (4), 2075-2089.
60. Quinto, C. A.; Mohindra, P.; Tong, S.; Bao, G., Multifunctional Superparamagnetic Iron Oxide Nanoparticles for Combined Chemotherapy and Hyperthermia Cancer Treatment. *Nanoscale* **2015**, *7* (29), 12728-12736.
61. Guo, H.; Chen, W.; Sun, X.; Liu, Y.-N.; Li, J.; Wang, J., Theranostic Magnetoliposomes Coated by Carboxymethyl Dextran with Controlled Release by Low-frequency Alternating Magnetic Field. *Carbohydr. Polym.* **2015**, *118*, 209-217.
62. Babincová, M.; Cicmanec, P.; Altanerová, V.; Altaner, C.; Babinec, P., AC-Magnetic Field Controlled Drug Release from Magnetoliposomes: Design of a Method for Site-Specific Chemotherapy. *Bioelectrochemistry* **2002**, *55* (1-2), 17-19.
63. Qiu, D.; An, X., Controllable Release from Magnetoliposomes by Magnetic Stimulation and Thermal Stimulation. *Colloids Surf., B* **2013**, *104*, 326-329.

64. Sadhukha, T.; Niu, L.; Wiedmann, T. S.; Panyam, J., Effective Elimination of Cancer Stem Cells by Magnetic Hyperthermia. *Mol. Pharmaceutics* **2013**, *10* (4), 1432-1441.
65. Shah, S. A.; Aslam Khan, M. U.; Arshad, M.; Awan, S. U.; Hashmi, M. U.; Ahmad, N., Doxorubicin-Loaded Photosensitive Magnetic Liposomes for Multi-Modal Cancer Therapy. *Colloids Surf., B* **2016**, *148*, 157-164.
66. Szoka, F.; Papahadjopoulos, D., Procedure for Preparation of Liposomes with Large Internal Aqueous Space and High Capture by Reverse-Phase Evaporation. *Proc. Natl. Acad. Sci. U. S. A.* **1978**, *75* (9), 4194-4198.
67. Akbarzadeh, A.; Rezaei-Sadabady, R.; Davaran, S.; Joo, S. W.; Zarghami, N.; Hanifehpour, Y.; Samiei, M.; Kouhi, M.; Nejati-Koshki, K., Liposome: Classification, Preparation, and Applications. *Nanoscale Res. Lett.* **2013**, *8* (1), 102.
68. Brollo, M. E. F.; Veintemillas-Verdaguer, S.; Salvan, C. M.; Morales, M. P., Key Parameters on the Microwave Assisted Synthesis of Magnetic Nanoparticles for MRI Contrast Agents. *Contrast Media Mol. Imaging* **2017**, *2017*, 13.
69. Roca, A. G.; Veintemillas-Verdaguer, S.; Port, M.; Robic, C.; Serna, C. J.; Morales, M. P., Effect of Nanoparticle and Aggregate Size on the Relaxometric Properties of MR Contrast Agents Based on High Quality Magnetite Nanoparticles. *J. Phys. Chem. B* **2009**, *113* (19), 7033-7039.
70. Kuntsche, J.; Horst, J. C.; Bunjes, H., Cryogenic Transmission Electron Microscopy (cryo-TEM) for Studying the Morphology of Colloidal Drug Delivery Systems. *Int. J. Pharm.* **2011**, *417* (1), 120-137.



Drug loaded magnetoliposomes prepared in one step could be used for an efficient drug release on demand at a specific time and place using an external AMF, reducing or even eliminating side effects.

77x96mm (300 x 300 DPI)

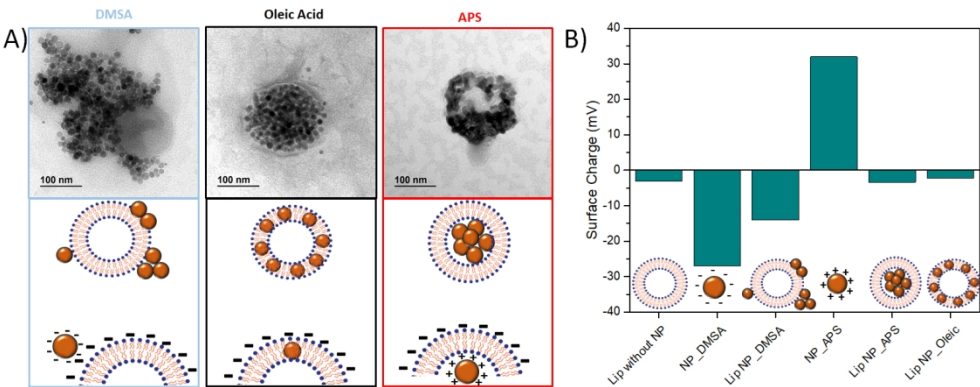


Figure 1

438x170mm (96 x 96 DPI)

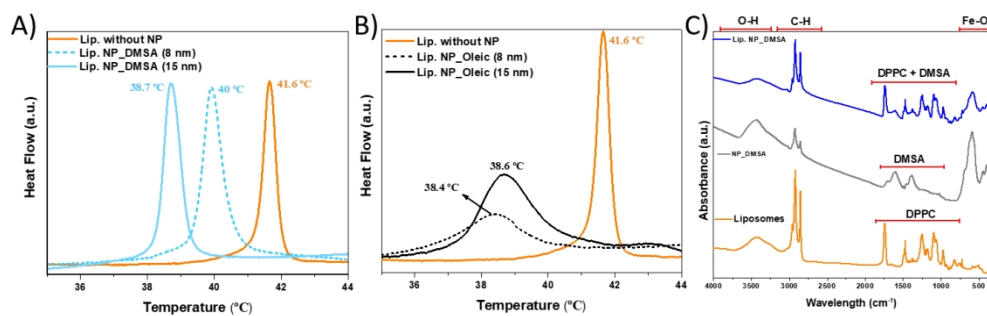


Figure 2

263x82mm (144 x 144 DPI)

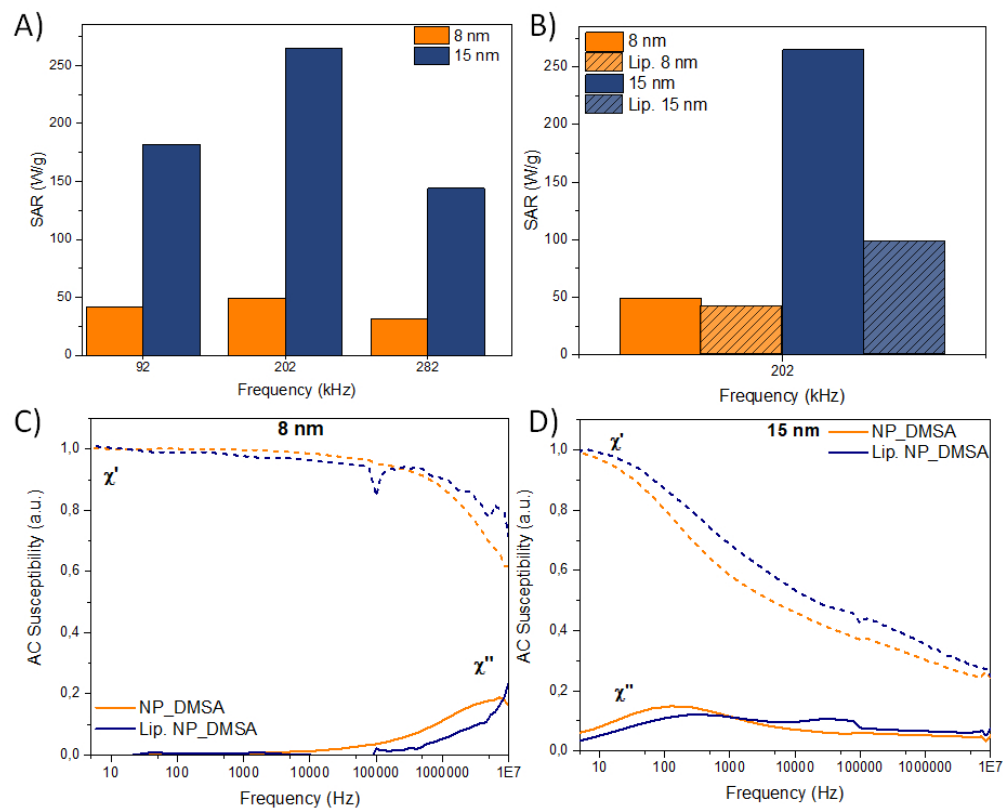


Figure 3

162x132mm (144 x 144 DPI)

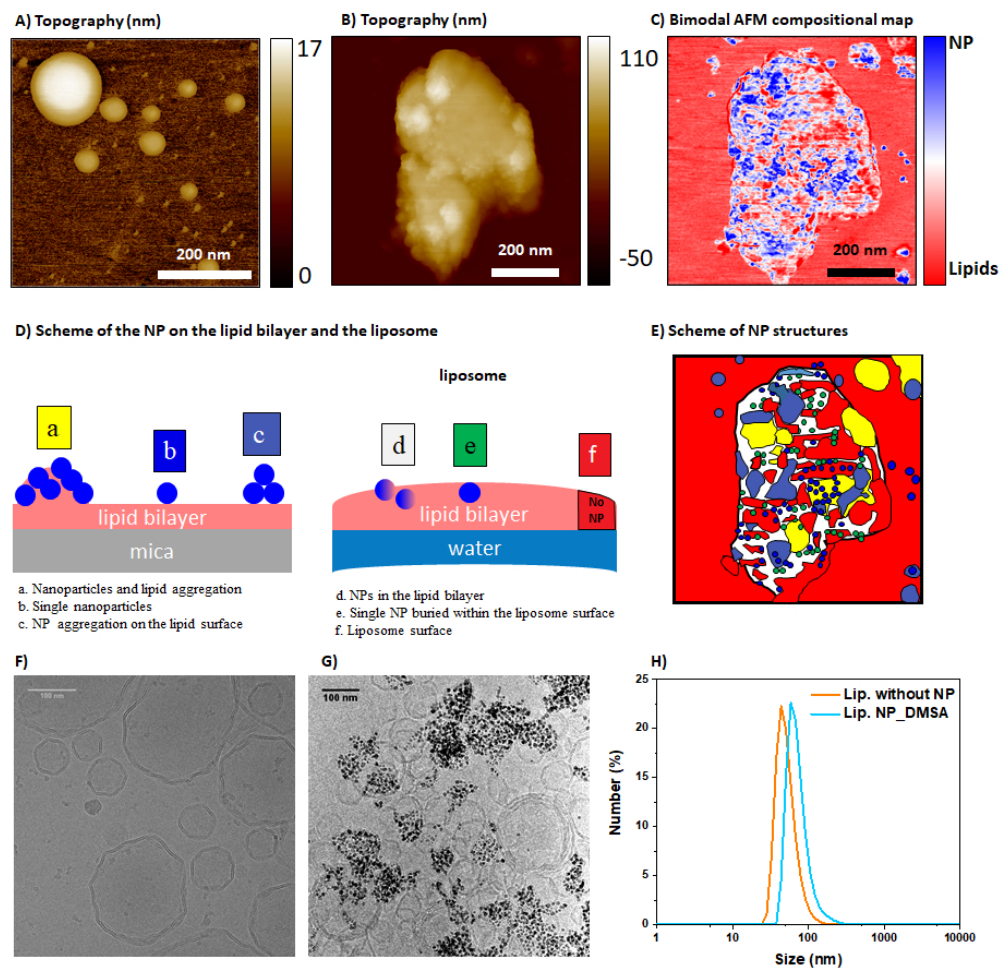


Figure 4

161x158mm (144 x 144 DPI)

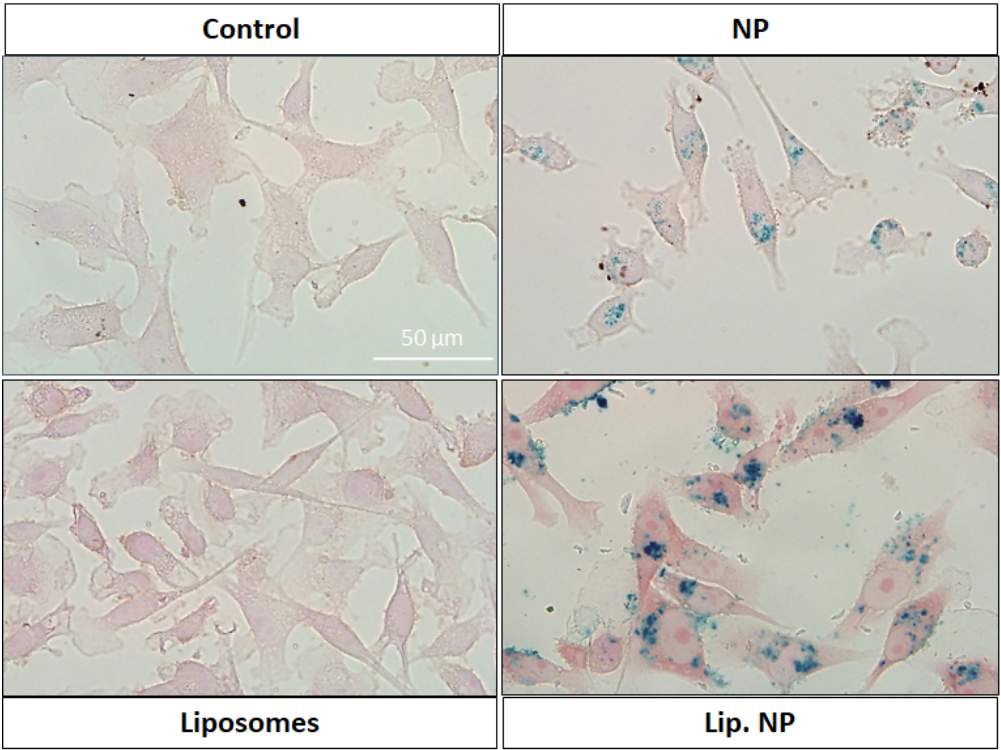


Figure 5
202x152mm (96 x 96 DPI)

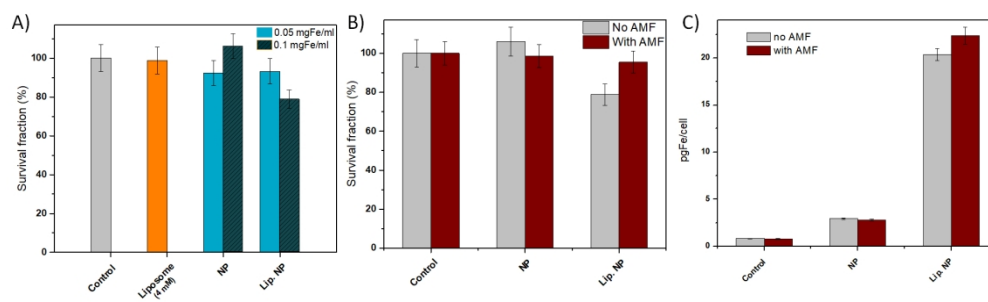


Figure 6

353x104mm (144 x 144 DPI)

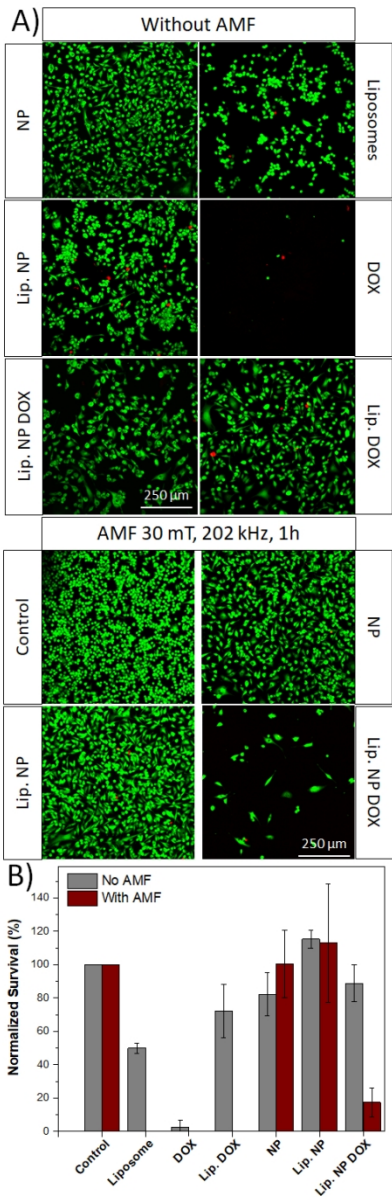


Figure 7

91x269mm (144 x 144 DPI)

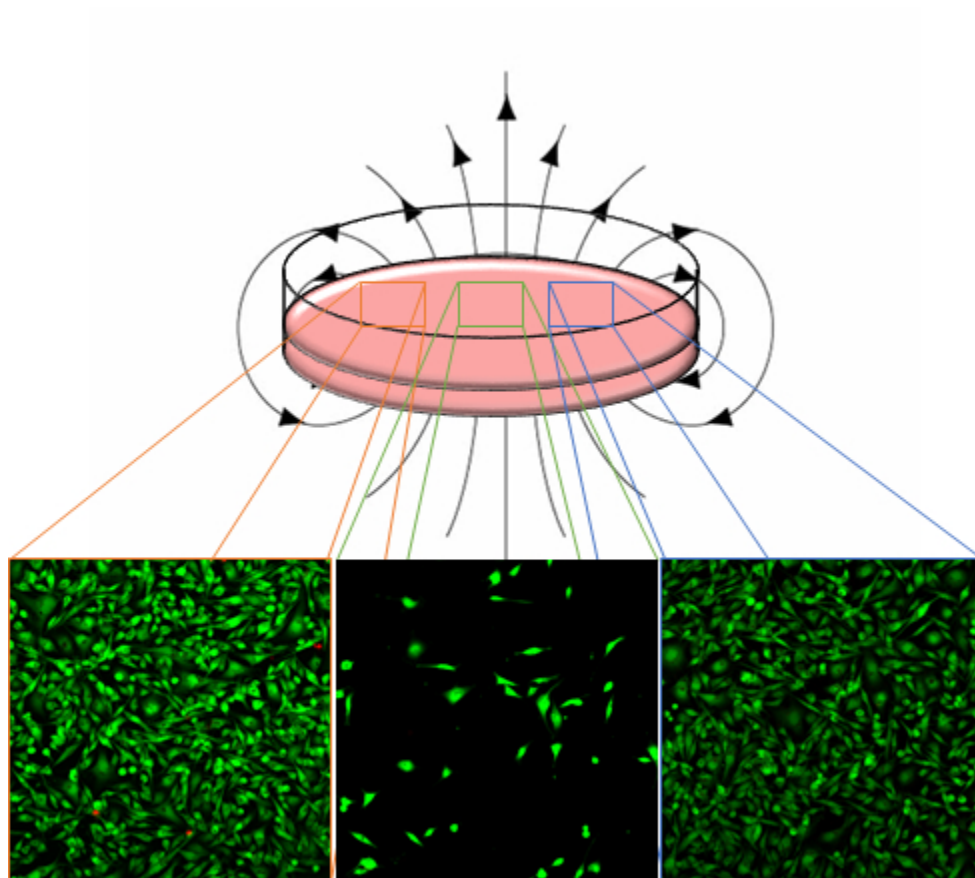


Figure 8

130x116mm (96 x 96 DPI)